Accelerated laboratory simulation of field aging for paving binders using hydrogen peroxide and UV light

Khalighi, Sadaf; Ma, Lili; Varveri, Aikaterini

DOI
10.1016/j.conbuildmat.2025.141272

Publication date
2025

Document Version
Final published version

Published in
Construction and Building Materials

Citation (APA)
Khalighi, S., Ma, L., & Varveri, A. (2025). Accelerated laboratory simulation of field aging for paving binders using hydrogen peroxide and UV light. *Construction and Building Materials*, *476*, Article 141272. https://doi.org/10.1016/j.conbuildmat.2025.141272

Construction and Building Materials 476 (2025) 141272

Contents lists available at ScienceDirect

Construction and Building Materials

journal homepage: www.elsevier.com/locate/conbuildmat

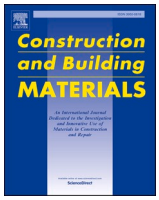

Accelerated laboratory simulation of field aging for paving binders using hydrogen peroxide and UV light

Sadaf Khalighi *, Lili Ma, Aikaterini Varveri

Delft University of Technology, Stevinweg 1, Delft 2628 CN, the Netherlands

ARTICLE INFO

Keywords:
Bituminous binder aging protocol
UPA
PAV
VBA
Hygrothermal aging
FTIR
DSR
Deconvolution
PCA
DTW

ABSTRACT

Developing a rapid and realistic binder aging protocol remains a challenge in pavement engineering. This study introduces the UV-Peroxide Aging (UPA) protocol, which employs hydrogen peroxide and UV light to accelerate oxidative reactions. The effects of hydrogen peroxide concentration, temperature, and aging duration were evaluated and compared with existing laboratory protocols and long-term field aging. Results show that UPA aging at 85°C for 3 h or 60°C for 6–9 h produces aging effects comparable to 9 years of field exposure. Additionally, new methods for lab-field comparisons of chemical and rheological properties were applied, offering a systematic framework for analysing optimized aging protocols.

1. Introduction

Road sustainability plays a crucial role in minimizing environmental impact, conserving resources, and enhancing the long-term performance of infrastructure [1]. A significant factor influencing road sustainability is binder aging, which leads to an increase in the stiffness of asphalt mixtures and a higher susceptibility to cracking [2]. This deterioration ultimately reduces the durability of the road and escalates maintenance requirements [3]. Binder aging occurs progressively during the construction phase, referred to as short-term aging (STA), and continues over its service life, termed long-term aging (LTA), when binder is exposed to traffic loads and environmental influences such as temperature fluctuations, moisture, and UV radiation [4].

For more sustainable road construction and maintenance, accurate predictions of binder properties after both STA and LTA are essential. To simulate these aging processes, pavement engineers commonly use laboratory aging protocols [5], with the Rolling Thin Film Oven Test (RTFOT) mainly utilized for STA and the Pressure Aging Vessel (PAV) for LTA [6–8]. The RTFOT method involves subjecting binder films to controlled airflow at 163 °C for 75 minutes (EN 12607–1, 2014) [9]. For the PAV method, bitumen films are aged in a pressurized vessel at 2.07 MPa and temperatures between 90 and 110 °C over a 20-hour period (EN 14769, 2012) [10].

The RTFOT and PAV aging protocols, while prevalent, continue to show limitations in accurately replicating field aging [11]. Standard RTFOT and PAV methods are intended to represent 5–10 years of field aging, while studies have shown that they underestimate field aging in many cases [12,13]. For instance, Lu et al. (2008) reported notable differences in chemical functional groups between field-aged and laboratory-aged binders [14], suggesting that the laboratory procedures do not fully capture the oxidative aging mechanisms occurring in real pavements. Similarly, Jing et al. (2019) observed that field aging in porous asphalt over three years was substantially harsher than laboratory aging using the standard RTFOT and PAV methods [15]. One proposed approach to overcome this problem is the extension of PAV aging duration. Singhvi et al. (2022) demonstrated that double PAV treatment could approximately replicate 8–12 years of aging in Illinois pavements, though differences between laboratory and field aging were still evident [16].

The discrepancies between chemical changes caused by field and laboratory aging mainly arise from their different aging conditions. Laboratory aging protocols primarily incorporate factors such as temperature, pressure, and time [11,17]. However, real-world conditions also include moisture, UV light, and reactive oxygen species (ROS), which are often omitted in standard protocols, even though these factors play a significant role in field aging.

* Corresponding author.
E-mail address: s.khalighi@tudelft.nl (S. Khalighi).

https://doi.org/10.1016/j.conbuildmat.2025.141272
Received 15 January 2025; Received in revised form 6 March 2025; Accepted 7 April 2025
Available online 13 April 2025

Research on moisture's impact on bitumen aging is not conclusive. Khalighi et al. [17] showed that combined thermal and moisture aging, or hygrothermal aging, accelerates aging more significantly than thermal aging alone, and it replicates field aging better than thermo-oxidative aging [17,29]. While some studies suggest minimal effects of moisture on bitumen aging [30] or variability in moisture' impact on aging among binder types [31].

Many studies have demonstrated the effects of UV light aging on binder chemical and rheological properties. These chemo-rheological changes occur over a significantly longer period than other laboratory aging methods, such as PAV protocol, which lasts 20 h. Menapace et al. [18] observed substantial chemical changes in binders exposed to UV radiation (0.89 W/m^2/nm at 340 nm) over 388 days, especially under dry conditions. Crucho et al. [19] simulated outdoor conditions with UV radiation and water/dry cycles for 30 days, observing a degrading effect on rheological properties such as increased stiffness, reduced phase angle, and diminished fatigue life. While UV aging induces notable chemical and rheological changes, its effectiveness in replicating field aging remains uncertain. On one hand, UV exposure occurs naturally in pavements and may better simulate certain aspects of field aging, particularly in surface layers. Wu et al. [20] noted a strong correlation between UV aging at specific thicknesses and natural exposure aging tests. On the other hand, UV aging is limited by its shallow penetration depth [21,22]. This leads to significantly decreased aging effects of UV radiation with increasing depth, primarily due to the formation of an impermeable surface layer on the asphalt binder samples. This limited the penetration of oxygen, resulting in less severe aging compared to thermal aging [22]. Furthermore, the aging effects of UV radiation depend on wavelength, with UV in the 300–350 nm range causing the most significant impact, while visible light also contributes to oxidation, particularly through blue and green wavelengths affecting carbonyl and sulfoxide formation as demonstrated by Mirwald et al. [23].

The ROS in the atmosphere include mainly ozone (O_3) and nitrogen oxides (NO_x), among other compounds. Ozone forms through the oxidation of hydrocarbons and carbon monoxide, while NO_x emissions come from car engines, commonly existing in environments near asphalt pavements [24,25]. To better simulate field aging, Mirwald et al. developed the Viennese Binder Aging (VBA) method by introducing ROS into the laboratory aging process, in which samples are exposed to air enriched with O_3 and NO_x for 72 h [26]. Hofko et al. found significant aging only in the presence of NO_x [27], and confirmed that NO_2 induced significant aging even at low concentrations, while O_3 had a milder effect [28]. A comparison between the application of aging protocols multiple times and field data showed that VBA provided a better approximation of field aging than standard methods by providing better simulation of chemical and rheological properties [28]. Despite the success of VBA, it still requires a specific STA protocol, which involves aging of a 0.5 mm binder film at 163°C for 5 h (pre-VBA), followed by longer aging durations of 72 h due to the slower diffusion of ROS in the gas phase at atmospheric pressure. Additionally, it does not account for the effects of UV light that is present in natural field aging [28].

Despite extensive research and modifications to laboratory aging protocols to incorporate additional environmental factors, accurately replicating field aging remains a challenge. Existing protocols are either too time-consuming or fail to replicate the chemical and rheological mechanisms of field aging accurately. A new aging protocol is needed to achieve a balance between efficiency and fidelity in simulating real-world asphalt binder aging.

2. Objective and methodology

The research aims to develop a more efficient laboratory binder aging method for more accurate simulation of field aging. This new protocol, referred to as the UV-Peroxide Aging (UPA) protocol, combines the use of UV light and hydrogen peroxide (H_2O_2) to generate highly reactive hydroxyl radicals (HO• and HO_2•) in liquid medium, leading to an accelerated aging process and an improved simulation of field aging mechanisms.

The combined use of UV and H_2O_2 has been widely implemented in environmental processes, such as wastewater treatment [32,33], due to its ability to generate hydroxyl radicals—among the most powerful reactive species, with an oxidation potential of 2.8 V, surpassing that of ozone (2.1 V) [34]. Based on this, we anticipate that hydroxyl radicals generated from the photodecomposition of H_2O_2 under UV light may act as catalysts, accelerating the oxidation aging of bituminous binders. Moreover, the generated radicals are present in water medium, which probably facilitates their diffusion and penetration into the binder, further accelerating the aging process. These radicals, which naturally occur in the field environment of asphalt pavements [35], offer a unique opportunity to simulate field-like aging mechanisms in the laboratory. Based on the current knowledge, there is no study investigating the effect of hydroxyl radicals on binder oxidative aging.

To optimize the UPA method, we will assess the impact of UV + H_2O_z on the aging of bituminous binders under various conditions, including different H_2O_2 concentrations and varying aging temperatures. To evaluate the effectiveness of the UPA protocol, other aging protocols, including PAV, VBA, and modified versions of these protocols under humid conditions, were tested for comparison, focusing on the chemical and rheological properties measured by Fourier Transform Infrared (FTIR) spectroscopy and dynamic shear rheometer (DSR). The moisture-modified versions of PAV and VBA protocols were included to ensure a more accurate comparison, as the UPA method takes place also in a water-containing environment. Furthermore, field-aged binder samples will be used as a benchmark to develop and refine the UPA method.

Several analytical methods will be utilized to effectively compare various aging protocols. To compare how rapidly different protocols induce aging, the aging rate indices will be proposed and calculated based on the chemical- and rheological properties. To assess the similarity of laboratory aging reactions to field aging, multivariate analysis methods, including Principal Component Analysis (PCA), the combined FTIR spectral deconvolution and Dynamic Time Warping (DTW), and Euclidean distance were employed to quantify the chemical differences between samples at various aging conditions using FTIR parameters including peak positions and areas. These techniques provide valuable tools for future comparisons between laboratory and field aging.

3. Materials and methods

3.1. Materials

In this study, two PEN 70/100 bituminous binders from different suppliers and thus from different crude oil sources were used, labelled as Q and T [17]. Table 1 shows their main basic properties. The Q and T binders were selected due to their widespread use in the Netherlands as 70/100 penetration grade binders, the availability of field-aged Q binder samples for direct comparison with laboratory aging, and the distinct elemental compositions between Q and T despite having the same penetration grade, enabling an assessment of compositional effects on

Table 1
Specifications of Q 70/100 and T 70/100 at fresh (unaged) state.

Property		Unit	Q PEN 70/100	T PEN 70/100
Penetration at 25 °C		0.1 mm	70–100	70–100
Softening point		°C	43–51	43–51
Complex shear modulus at 1.6 Hz & 60 °C		kPa	1.8	2.3
Phase angle at 1.6 Hz & 60 °C		°	88	88
Chemicals	Nitrogen N	(%)	0.59	0.93
	Carbon C		79.19	87.23
	Hydrogen H		10.81	11.26
	Sulfur S		4.47	3.35
	Oxygen O		2.25	0.60

aging behaviour. These binders serve as the foundational materials for developing our aging protocols, with future studies planned to incorporate a broader range of binder types to enhance the generalizability of the findings.

3.2. Sample preparation and aging conditions

Binder samples were tested in different aging states: unaged (fresh), short-term aged (STA), and long-term aged (LTA). To conduct STA, 50 g of each fresh binder were poured into pans to produce films with a thickness of 3.2 mm. These pans were subjected to a short-term aging (STA) process using oven aging at 163°C for 5 h, following the Thin Film Oven (TFO) procedure according to EN 12607–2 [9], simulating the aging during production and construction phases. The LTA samples were prepared by pouring TFO-aged binder into petri dishes to achieve 1 mm thickness, except for the standard PAV, which used a 3.2 mm film. The uniformity of the LTA films was ensured by heating the petri dishes at 163°C for 3 minutes. These samples were then subjected to five different aging protocols, namely UPA(H_2O_2 +UV), VBA-DRY, VBA-WET, PAV-STD, PAV-MOD, as listed in Table 2. For more details about sample preparation, please refer to our previous study [17].

For UPA (H_2O_2 + UV) aging, the Atlas XXL+ weatherometer was used to age 1 mm binder films at different H_2O_2 concentrations (12 % and 33 %) and temperatures (60, 70, 85 °C) for 3 h. Additional tests at 60 °C for longer durations of 6 and 9 h were also conducted. Furthermore, two control groups, namely UV and OVEN, were also prepared for comparison, each including samples aged both at 60 °C for 9 h and 85 °C for 3 h, the former conducted in the weatherometer with UV but without H_2O_2; and the latter in an oven without UV or H_2O_2. The H_2O_2 was directly applied on top of the binder films, and the sample pan with binder and H_2O_2 was then sealed to prevent the evaporation of H_2O_2. The H_2O_2 concentrations of 12 % and 33 % were chosen for their commercial availability, relevance in oxidative stress research in wastewater treatment, their common use in research and industry, and for studying the effects of varying concentrations, while ensuring these concentrations remain within the safe operational range. The UV light source in the weatherometer was centered at 340 nm (range 300–400 nm) with an intensity of 40 W/m^2. The irradiance distribution across all sample surfaces was uniform, as ensured by the design of the commercial weatherometer. The UV source-to-sample distance was fixed at 37 cm and remained constant throughout the study. Different temperatures were achieved through the chamber's heating system. However, due to the black colour of binder films, they absorb more UV energy than the surrounding air, leading to slightly higher temperatures than the chamber setting. Therefore, to ensure binder film temperatures of 60, 70, and 85 °C, the chamber temperature was set to lower temperatures 40, 50, and 65 °C, respectively, which have been confirmed through monitoring sample surface temperatures during aging process. Humidity in the chamber was maintained at minimum level possible (<10 % relative humidity) for all tests.

Furthermore, the Viennese Binder Aging (VBA) method was employed, using air enriched with 25 ppm NO_2 and 4 g/m^3 ozone at 85 ± 1°C for three days (VBA-DRY). A variant (VBA-WET) was also conducted by introducing 75 g/m^3 humidity via water spray, while keeping all other conditions the same [36].

Standard PAV (PAV-STD) aging was conducted at 90 °C, 20 bar, with a 3.2 mm film for 20 h. A modified PAV (PAV-MOD) with > 99 % relative humidity at 85 °C, 20 bar for 20 h was also tested. Humidity was introduced using 1000 g of demineralized water. Further details regarding setting humidity in PAV chamber can be found in [17].

Additionally, a field-aged sample (Field-9y) using Q bitumen as the binder, representing 9 years of aging in porous asphalt, was included for comparison. Details on its preparation, aging, and extraction details are available in [29].

3.3. Fourier Transform Infrared (FTIR) spectroscopy

FTIR samples were prepared following Mirwald et al. [26]. Spectral measurements were taken using a Nicolet iS5 Thermo Fisher Scientific instrument with an attenuated total reflection unit, generating each spectrum from 24 scans at a resolution of 4 cm^{-1} over the range of 4000–400 cm^{-1}, with four replicates per sample. To ensure the accuracy and comparability of ATR-FTIR spectral data, baseline correction and normalization were applied. Baseline correction was performed using an eight-point method as recommended by RILEM [37] (Table 1S). Normalization was then applied to scale all spectra between 0 and 1 [17, 38]. This step facilitates direct comparisons by minimizing variations in overall spectral intensity due to different operational conditions such as load force and sample thickness. The equations used for these corrections are provided in the supporting information.

Important peaks and their corresponding wavenumber ranges, along with the functional groups they represent are detailed in Table 3. The index for each functional group was calculated by dividing the integrated area under the curve within the peak ranges (A_x) mentioned in Table 3 over summation of all areas (A_{total}), following the equation:

$$\text{index} = A_x / A_{\text{Total}} \quad (1)$$

3.4. Dynamic shear rheometer (DSR) - frequency sweep

The dynamic shear rheometer (DSR) tests were performed with an 8-mm-diameter parallel plate and a 2-mm gap at temperatures from 0 to 40°C (10°C steps), across a frequency range of 15.9–0.0159 Hz (100–0.1 rad/s), with strain loads of 0.05 % and 0.1 % for 0–20°C and 30–40°C, respectively. Based on the time-temperature superposition principle (TTSP), master curves of complex shear modulus (G*) and phase angle (δ) were constructed at a reference temperature of 20°C

Table 2
Aging conditions for binder samples.

Aging protocol	Thickness (mm)	Temperature (°C)	Pressure (bar)	Relative humidity	Accelerator reactant	Time (Hours)	nomenclature	# of samples
UPA (H2O2 +UV)	1	60, 70, 85	1	Binder covered by liquid	12 % or 33 % H_2O_2 + UV	3	Q−12 %-70C-3H	12
	1	60	1	Binder covered by liquid	12 % or 33 % H_2O_2 + UV	6, 9	Q−33 %-60C-9H	8
OVEN (Control groups for UPA)	1	60, 85	1	-	without UV or H_2O_2	3, 9	Q/T-OVEN-60C-9H	4
UV (Control groups for UPA)	1	60, 85	1	-	UV, without H_2O_2	3, 9	Q/T-UV-85C-3H	4
PAV-STD	3.2	90	20	-	Pressure, temperature	20	Q/T-PAV-STD	2
PAV-MOD	1	85	20	> 99 % humidity	Pressure	20	Q/T-PAV-MOD	2
VBA-DRY VBA-WET	1	85	1	< 10 % or ~21 % humidity	NO_2 and ozone	72	Q/T-VBA-DRY/WET	4

Table 3
Main functional groups of binder identified in FTIR spectra [39].

Area	Band range (cm^{-1})	Functional groups
A810	710–734 734–783 783–833 833–912	Hydrocarbon chain, $(CH_2)_n$, C–H in isolated/two/four adjacent hydrogen aromatic rings or C–CH_2 rocking in alkyl side chains with more than four carbons
A1030	984–1047	Oxygenated function-sulfoxide, S═O
A1200	1100–1180 1280–1330	Tertiary alcohol C-C-O, C-O in carboxylic acid, C-C-C in diaryl ketones, C-N secondary amides, O═S═O in sulfone
A1376	1350–1395	Branched aliphatic structures, CH_3
A1460	1395–1525	Aliphatic structures, CH_3 and CH_2
A1600	1535–1670	Aromatic structure, C═C
A1700	1660–1750	Oxygenated function-carbonyl, C═O
A2953	2820–2880 2880–2990	Aliphatic structures, Symmetric, Asymmetric stretching, CH
A3400	3100–3600	Hydroxyl stretching, OH, NH
A total = A 810 + A 1030 + A 1200 + A 1376 +A 1460 + A 1600 +A 1700 +A 2953 + A3400		

[17]. All measurements followed standard testing protocols (NEN-EN 14770 [40]).

3.5. Principle component analysis (PCA)

PCA is a key technique for reducing dataset dimensionality by transforming variables into uncorrelated principal components. The transformation is expressed as $\mathbf{Y}=\mathbf{X}\times\mathbf{W}$, where $\mathbf{X}$ is the dataset of m samples and n variables; $\mathbf{W}$ is the loading or transforming matrix of size $n\times p$, with p representing the number of principal components; the score matrix $\mathbf{Y}$, of size $m\times p$, represents the lower-dimensional projection of $\mathbf{X}$.

PCA was employed to compare the similarity between samples at various aging conditions based on their chemical properties, specifically the 10 FTIR indices, listed in Table 3. By compacting the FTIR dataset into a smaller set of principal components while preserving essential information, PCA helps overcome the "curse of dimensionality" that arises when analysing all FTIR indices simultaneously. This dimensionality reduction makes it easier to visualize clustering patterns—where closer clustering indicates more similar chemical properties—and to distinguish between different aging conditions. For more details regarding PCA, please refer to reference [17].

3.6. Pairwise Euclidean distance

Pairwise Euclidean distance is a metric that quantifies the straight-line distance between each pair of points in a dataset within a multi-dimensional Euclidean space (which can be described by the coordinate system). The Euclidean distance between two points $(p_1,p_2,\ldots,p_d)$ *and* $(q_1,q_2,\ldots,q_d)$ can be calculated according to Eq. 2:

$$\textit{Euclidean distance} = \sqrt{((p_1-q_1)^2+(p_2-q_2)^2+\ldots+(p_d-q_d)^2} \quad (2)$$

where: p_i and q_i represent the coordinates (or feature values) of two data points in a d-dimensional space, d is the number of dimensions (or variables) used in the comparison. Similar to our previous studies [17], to determine which laboratory conditions most closely replicate the field aging, the Euclidean pairwise distance, were computed based on the first two principal components [41].

3.7. Deconvolution of FTIR spectra

A key challenge in applying FTIR to complex materials like bituminous binder is the issue of spectral overlap [31]. The close proximity of functional group bands can complicate both qualitative and quantitative analysis, especially after aging when more functional groups occur. To address this, deconvolution of FTIR spectra is employed [32]. Deconvolution is an analytical technique that separates complex infrared spectra into individual vibrational components, enhancing spectral resolution and isolating overlapping peaks [31,32]. This method enables the extraction of detailed molecular and chemical information, providing a deeper understanding of the chemical structures and interactions within the binder. For FTIR deconvolution, the spectral data pre-processed by baseline correction and normalization were used. Peak identification was initially carried out by analysing first and second derivatives. Primary peaks were identified at the positions where the first derivative changes sign, while secondary peaks were located at the points where the second derivative changes sign. Subsequently, each identified peak was simulated by a Gaussian curve, characterized by its position (wavelength), height (intensity), and width (standard deviation) [37]. A spectral region with overlapping peaks was then fitted by comparing it to a sum of multiple gaussian curves, using the scipy.optimize.least_squares function in Python. To avoid fitting too many unknown parameters at once and to improve fitting efficiency and accuracy, the entire FTIR spectrum was divided into several segments, with each segment deconvoluted separately. The deconvoluted peaks were then compared with peak interpretation results from FTIR databases or literature [42], ensuring accurate fitting of peaks and proper interpretation of their corresponding functional groups.

3.8. Dynamic time warping (DTW)

The similarity between laboratory-aged and field-aged samples was assessed using deconvoluted peaks from FTIR spectra. However, variations in aging conditions can lead to peak shifts and differences in peak numbers between samples, making conventional distance metrics like Euclidean distance unsuitable for direct comparison. To address this, the Dynamic Time Warping (DTW) algorithm was employed due to its ability to accommodate temporal shifts and non-linear variations in spectral data. DTW ensures that spectral peaks corresponding to the same chemical functional groups are properly aligned, enabling a meaningful comparison of oxidation-related changes between lab-aged and field-aged samples. Once the spectral features were aligned, the Euclidean distance was calculated based on the areas under the aligned peaks, providing a quantitative measure of oxidation similarity. This approach allowed us to evaluate how well the laboratory aging protocol replicates field aging by comparing the oxidation levels in lab-aged samples relative to field-aged ones.

To apply DTW, the deconvoluted peak positions were treated as time series data, with each peak position representing a distinct time point in the sequence.

The spectral data from the field-aged sample served as the reference data, denoted as $\mathbf{T}$ with a length of I, while the laboratory-aged sample data served as the training data, denoted as $\mathbf{S}$ with a length of J.

The DTW process begins by constructing a two-dimensional distance matrix, where each element $d(i,j)$ represents the Euclidean distance between the i-th peak position in the reference data $\mathbf{T}$ and the j-th peak position in the training data $\mathbf{S}$ [43–45]. The algorithm then searches for the optimal warping path D that minimizes the cumulative distance between two data, thus achieving the best alignment[43]. The optimal path is defined as:

$$D=\sum_{q=1}^{Q} d(i(q),j(q)) \text{ where} q \text{is a step index along the path} \quad (3)$$

Where D is the total alignment cost along the optimal warping path. $d(i,j)$ is the Euclidean distance between the i-th peak position in the reference dataset $\mathbf{T}$ and the j-th peak position in the training dataset $\mathbf{S}$. Q is the total number of steps in the optimal path. q is the step index along the path.

Here, the optimal path starts at the top-left corner and ends at the bottom-right corner of the matrix and maintains monotonicity and

continuity. This ensures that the path progresses consistently through the sequence of peak positions without looping back or skipping any spectral features [45].

Given the computational intensity of the classic DTW algorithm, particularly its quadratic time and space complexity, we employed an optimized version known as Fast-DTW. This method reduces computational complexity by approximating the optimal path through a series of key operations [45]. First, the original time series data is coarsened by down-sampling to produce a simplified representation. Second, the minimum-distance warp path is identified within this coarser resolution. Third, this warp path is refined by making local adjustments at progressively finer resolutions, thereby improving the accuracy of the alignment. This approach allowed for a linear time and space complexity, making it feasible to handle the FTIR data efficiently without sacrificing alignment accuracy. The DTW distance, representing the total alignment cost, was calculated by summing the Euclidean distances along the identified optimal path.

3.9. Cumulative aging and aging rate

When assessing the efficacy of aging protocols and determine the optimal aging protocol, it is crucial to consider both the cumulative aging and the rate of aging. Cumulative aging (CA) represents the overall extent of aging. A cumulative aging closely aligning field aging indicates an accurate replication of real-world conditions. On the other hand, the aging rate (AR), defined as the change rate of aging extent over time, offers insights into the dynamics of the aging process, highlighting how rapidly aging occurs. A higher aging rate allows for a faster assessment of materials aging behaviour, leading to significant saving of time and resources.

Chemical and rheological properties serve as robust indicators of material aging performance. In our analysis, we utilized both FTIR indices (10) and master curve data points (80 points at different frequencies and temperatures) to quantify the cumulative aging and aging rate indices. Cumulative aging based on chemical and rheological properties, denoted as CA_{che} and CA_{rhe}, was calculated as the summation of changes relative to the fresh condition using Eqs. 4 and 5, respectively. The aging rate, defined as AR_{che} and AR_{rhe} was calculated using Eqs. 6 and 7, respectively.

$$CA_{che} = \sum_{index=1}^{index10} \frac{|PI_{fresh} - PI_{aged}|}{PI_{fresh}} \tag{4}$$

Where PI_{fresh} and PI_{aged} are the FTIR peak index (*PI*) values for the fresh and aged samples, respectively.

$$CA_{rhe} = \sum_{i=1}^{80} \frac{\left|G^*_{i,fresh} - G^*_{i,aged}\right|}{G^*_{i,fresh}} + \sum_{i=1}^{80} \frac{|\delta_{i,fresh} - \delta_{i,aged}|}{\delta_{i,fresh}} \tag{5}$$

Where $G^*_{i,fresh}$and $G^*_{i,aged}$ represent the complex shear moduli, and $\delta_{i,fresh}$ and $\delta_{i,aged}$ denote the phase angles of the fresh and aged samples, respectively, at the *i*-th master curve data point.

The aging rate based on chemical and rheological parameters, represented as AR_{che} and AR_{rhe}, respectively, were calculated as:

$$AR_{che} = \frac{CA_{che}}{t} \tag{6}$$

$$AR_{rhe} = \frac{CA_{rhe}}{t} \tag{7}$$

Where *t* is the duration of the aging process (in hours).

3.10. Chemo-rheological correlation analysis

To quantify the relationship between chemical and rheological changes, a statistical correlation method, i.e., Pearson's correlation, was applied. Pearson's correlation coefficient (ρ), as described by Eq. 8, assesses the linear correlation between chemical and rheological parameters.

$$\rho_{xy} = \frac{Cov(x,y)}{\sigma_x \sigma_y} \tag{8}$$

where Cov(*x*,*y*) is covariance between variables *x*, and *y*, σ_x and σ_y are standard deviation of *x* and *y*, respectively. The correlation coefficient ranges from −1–1, with ρ= 1/-1 signifying a perfect positive/negative correlation.

4. Results and discussion

4.1. Aging effects on chemical properties

Fig. 1 presents the FTIR spectra of the Q binder subjected to various aging conditions, namely, short-term aging via the TFOT method and long-term aging, including OVEN, UV, UPA, PAV-STD, PAV-MOD, VBA-DRY, VBA-WET, and Field-9y. In Fig. 1a, the raw spectra show that VBA-DRY and VBA-WET are positioned at higher intensities compared to the other spectra, making direct comparisons challenging. This issue is resolved after baseline correction and normalization, as shown in Fig. 1b and c. The spectra indicate that different aging conditions affect the FTIR peaks to varying degrees. Notably, after baseline correction and normalization, the field-aged sample exhibits the most pronounced peak shifts, enabling us to properly evaluate the chemical changes in this sample. Importantly, the UPA aging protocol introduced in this study, which combines H_2O_2 and UV light, does not result in the appearance of new peaks in the spectra. This observation supports the hypothesis that radicals generated from the decomposition of H_2O_2 serve as catalysts, accelerating the oxidation process in a manner consistent with field aging. The validity of this hypothesis will be further investigated in detail by indices calculation and deconvolution analysis.

Fig. 2, a) - j) displays the ten FTIR indices at all aging conditions for both Q and T binders. The carbonyl and sulfoxide indices, identified as two most relevant FTIR indicators of aging levels, are specifically shown in a) and b). For both Q and T, UPA treatment increased carbonyl and sulfoxide indices for both 12 % and 33 % H_2O_2 concentrations, with a higher radical concentration led to more aggressive oxidation reactions especially at higher temperatures and longer durations. At 60°C, longer durations led to higher indices, indicating more aging. For a duration of 3 h, the highest temperatures of 85°C caused the largest increase in both indices. Time and temperature exerted varying aging impact at two concentrations: time had a stronger effect at 12 % H_2O_2, whereas temperature was more influential at 33 % H_2O_2.

The carbonyl and sulfoxide indices of other aging protocols are also presented in a) and b), including OVEN, UV, PAV-STD, PAV-MOD, VBA-DRY, VBA-WET, and Field-9y aging. For both Q and T, OVEN aging at 60°C for 9 h resulted in a similar carbonyl index and a slightly lower sulfoxide index compared to the aging at 85°C for 3 h. UV aging at 60°C for 9 h increased both indices slightly more than UV aging at 85°C for 3 h. As expected, adding humidity to PAV-STD and VBA-DRY increased carbonyl and sulfoxide indices, indicating that the combination of moisture and ROS accelerates the oxidative aging process. Compared to VBA-DRY, the T sampled aged by VBA-WET shows a much larger carbonyl index while for Q, the difference between VBA-DRY and VBA-WET is much smaller, indicating that the effect of moisture on aging process varies with binder type.

A comparison between UPA and other aging protocols revealed that, for both binders, exposure to a high concentration (33 %) of H_2O_2 at 60°C for 9 h and at 85°C for 3 h resulted in carbonyl indices similar to those of PAV-MOD and VBA-WET (except for the T binder aged under VBA-WET conditions). All these samples exhibited aging levels similar to that observed after 9 years of field exposure. This suggests that the UPA with high H_2O_2 for 3–9 h are comparable to 20 h of PAV and 3 days of

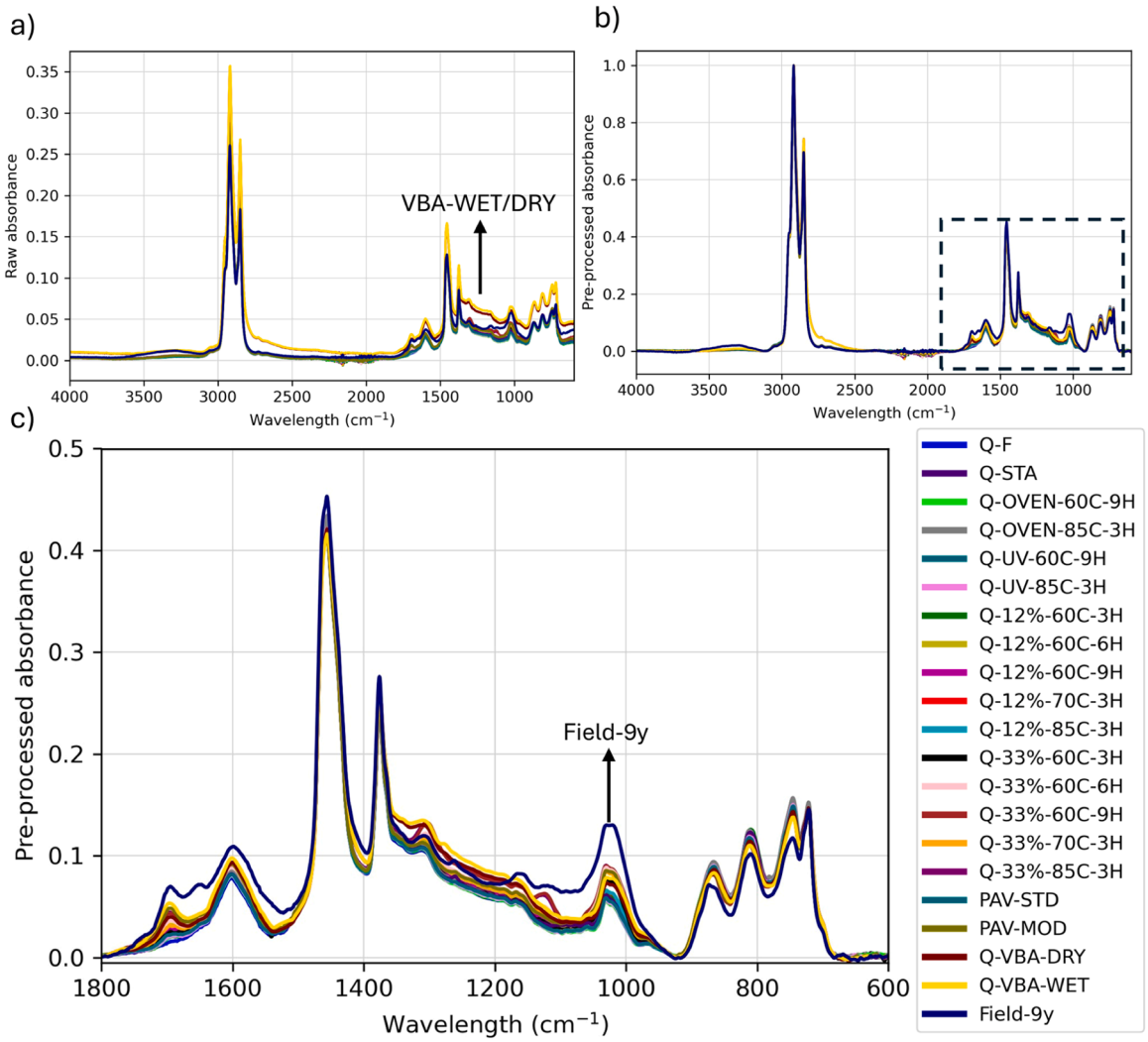

Fig. 1. FTIR spectra of fresh, short-term aged, long-term aged (including UPA, VBA,PAV, and a 9-year field aging) samples presented in: a) raw spectral form, b) baseline-corrected and normalized spectra, and c) the 600–1800 cm^{-1} region.

VBA methods and equivalent to approximately 8–9 years of field aging for porous asphalt.

Compared to Q binders, most T binders revealed a higher sulfoxide index. These differences between Q and T may be attributed to the binders' unique chemical composition Compared to Q, T binder contains lower oxygen and sulfur contents, higher nitrogen content, and a higher carbon-to-hydrogen ratio (indicating a higher degree of aromaticity and unsaturation), as shown in Table 1, which may undergo faster oxidation in the simultaneous presence of ROS and moisture. This suggests that the intrinsic chemical composition of the binder is an important factor affecting sensitivity of various binders to different aging factor combinations.

Furthermore, most T samples aged by UPA show higher carbonyl and sulfoxide indices than those of PAV and VBA methods, while for Q, the difference in both indices between UPA, PAV and VBA is smaller, suggesting that hydroxyl and perhydroxyl radicals contribute to more intense oxidation of sulfur- and carbon-containing species compared to conventional methods for T binders. This indicates that T binder is highly sensitive to ROS generated by H_2O_2+UV, leading to rapid changes in its chemical composition and aging.

Other indices showed trends similar to carbonyl and sulfoxide changes. The hydroxyl index (Fig. 2d) slightly increased for both binders, with T binder showing larger variation. Sulfones and aromatics indices (Fig. 2c and e) increased after both short-term and long-term aging. The sulfone region, representing sulfur-containing oxidation products, usually shifts to higher absorption with further aging. However, the absorption bands between 1350 and 1100 cm^{-1} may also arise from deformation vibrations of methylene and aromatic groups, or from skeletal vibrations of branched aliphatic motifs. To achieve a precise assignment of these overlapping bands, deconvolution of the FTIR spectra is necessary. This process will be discussed in detail later in this paper. Aging increases aromaticity, explaining the higher aromatics index after aging [46]. PAV-MOD, VBA-WET, and high concentration (33 %) UPA samples at 60°C for 9 h and 85°C for 3 h showed the highest aromatics index, indicating increased sensitivity to ROS and water vapor. This suggests that a higher H_2O_2 concentration promotes oxidative polymerization, leading to greater aromatic content in the aged binder.

The increase in aromaticity observed in aged samples aligns with the oxidative condensation of polycyclic aromatic hydrocarbons. As oxidation progresses, aliphatic components degrade, and smaller aromatic species polymerize, forming larger, more complex aromatic structures. This process contributes to the stiffening of bitumen and reduced ductility, which are characteristic of aged binders. The effect is particularly pronounced in PAV-MOD and VBA-WET samples, where moisture and elevated temperatures increase oxidation reactions, leading to further polymerization and structural rearrangement.

The aliphatic index (Fig. 2f) decreased after aging, with PAV-MOD,

Fig. 2. FTIR indices of Q and T binders at different aging conditions summarized in Table 2: a) carbonyl index, b) sulfoxide index, c) sulfone index, d) hydroxyl index, e) aromatic index, f) aliphatic index, and long chain indices in the range of g) 710–734 cm^{-1}, h) 734–783 cm^{-1}, i) 783–833 cm^{-1}, j) 833–912 cm^{-1}.

VBA-WET, and high concentration (33 %) UPA samples showing the strongest decreases, even more than 9 years of field aging. This suggests that increased ROS levels at higher H_2O_2 concentrations accelerate the breakdown of long-chain aliphatic structures. The long-chain indices (Fig. 2g - j) also declined in aged samples compared to fresh conditions, with VBA-DRY and VBA-WET showing further decreases below field aging levels for the 710–734 cm^{-1} range, indicating breakdown of long alkyl side chains. These four indices represent hydrocarbon chain, $(CH_2)_n$, C–H in isolated/two/four adjacent hydrogen aromatic rings or C–CH_2 rocking in alkyl side chains with more than four carbons.

The observed decrease in aliphatic indices suggests that oxidation preferentially targets long-chain hydrocarbons, leading to chain scission and fragmentation. This breakdown reduces the proportion of flexible aliphatic structures in bitumen, contributing to increased stiffness and brittleness. The enhanced degradation observed in VBA and UPA samples can be attributed to the combined effects of moisture and ROS, which increase oxidative cleavage of alkyl side chains. Such degradation mechanisms agree with the chemical transformations reported in field-aged binders, further supporting the validity of UPA as a laboratory aging method.

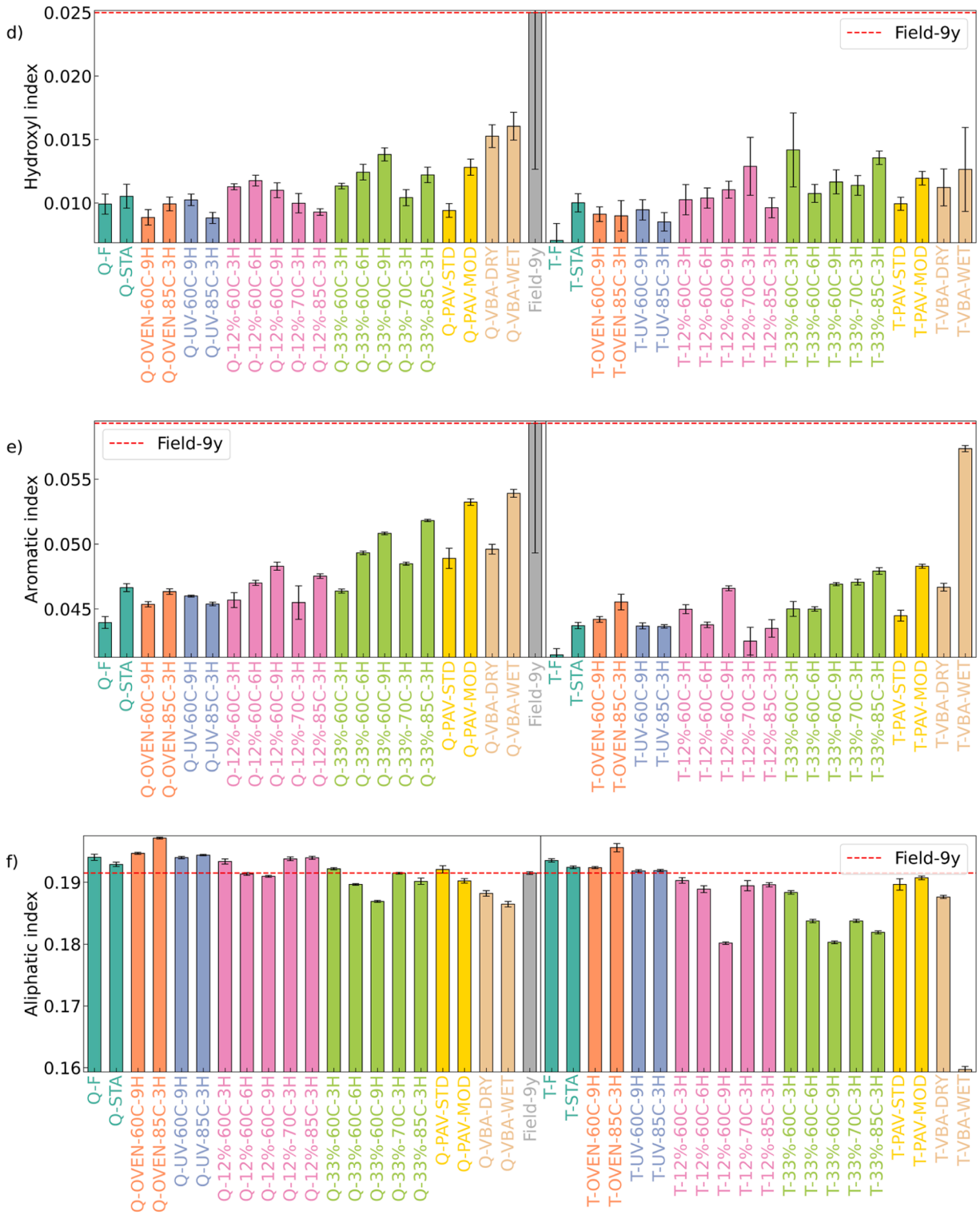

Fig. 2. (*continued*).

4.2. Cumulative aging and aging rate based on chemical properties

This work aims to develop an aging protocol with both high similarity to field aging and a fast aging rate. Therefore, cumulative aging (CA) and aging rate (AR) for different aging protocols were calculated based on all FTIR indices. Fig. 3a and b show the chemical CA for Q and T samples, respectively, aged by various protocols. For Q binders, no samples exhibited a CA> 4, while samples aged by VBA-WET, 33 %-60C-9H, and 33 %-85C-3H showed CA values higher than 3. For T binders, six samples showed a CA> 4, with VBA-WET,33 %-85C-3H, and 33 %-60C-9H revealing the highest three CA values. This indicates T binder's higher sensitivity to reactive species. The higher sensitivity of T binder to reactive species suggests a higher proportion of oxidation-prone components, such as aromatic fractions or unsaturated compounds, leading to a more rapid chemical change under aging conditions.

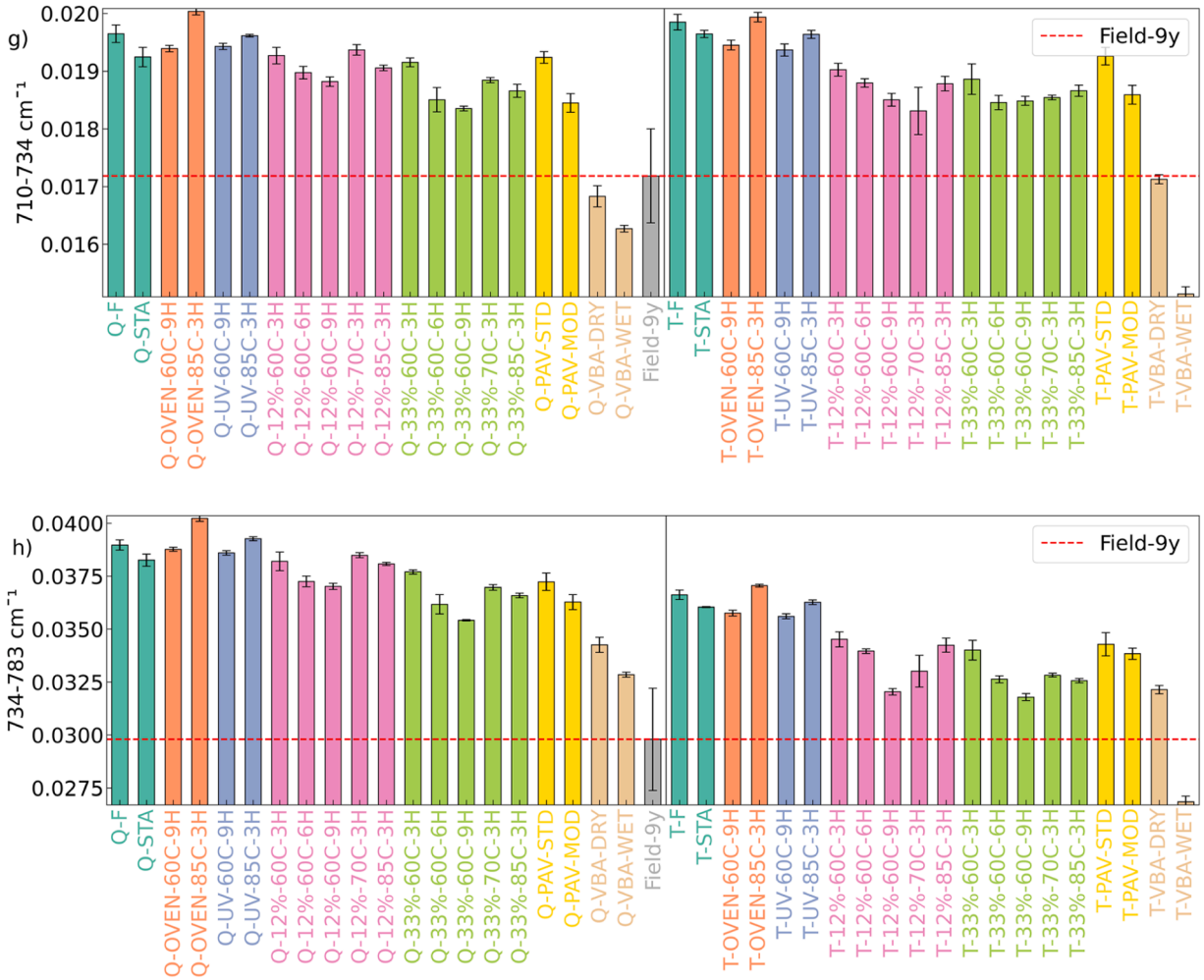

Fig. 2. (*continued*).

Fig. 3a and b also show the AR for Q and T binders, respectively. UPA for 33 %-85C-3H showed the fastest aging process, followed by UPA for 33 %-70C-3H for both binders. Other protocols had significantly lower aging rates, requiring longer aging times to achieve a high aging level. For example, PAV method (both STD and MOD) and VBA aging method (both DRY and WET) require 20 and 72 h, respectively, to simulate long-term aging, whereas the UPA method achieves comparable or even more pronounced aging effects within significantly shorter durations (e.g., 3–9 h). This enhanced efficiency is attributed to the higher oxidation potential of hydroxyl radicals and peroxides in UPA, which accelerate chemical changes that would otherwise require prolonged exposure to high pressure (such as PAV) or other ROS species (such as O_3 and NO_x in VBA method) [34]. Moreover, UPA employs liquid-phase oxidation, which facilitates the diffusion and penetration of oxidative agents into the binder, in contrast to PAV and VBA, which operates through gas-phase oxidation.

4.3. Comparison between field and laboratory aging using PCA, Euclidean distance, and FTIR indices

To further compare laboratory-aged samples with field-aged ones, PCA was utilized with all FTIR indices as inputs. The first two principal components explain over 85 % of the total variance (Fig. 1S), making a two-dimensional plot of PC1 versus PC2 a sufficient representation of the data, as shown in Fig. 4. The plot reveals that with laboratory aging, samples migrate from the upper left to the lower right, with an increase in PC1 and a decrease in PC2. Notably, the field-aged sample occupies a distinct position, separate from all lab-aged samples, and as aging progresses, the laboratory-aged samples exhibit more similar PC1 values to the field sample.

To identify FTIR indices important for distinguishing between field-aged and laboratory-aged samples, PCA loadings were analysed to quantify the contribution of each original variable (FTIR index) to the principal components. Loadings were normalized to a scale ranging from -1 to $+1$, with ± 0.8 as the threshold for significance. The positive/negative sign of a loading indicates a positive/negative relationship between the variable and the principal component, and the magnitude of the loading reflects the strength of the variable's influence on the principal component. This analysis focuses on high-magnitude loadings, regardless of their sign, as indicators of significant impact on the principal components.

Fig. 5 illustrates the normalized loading values for two principal components plotted in Fig. 4. For PC1, the long-chain region (734–833 cm^{-1}) and the aliphatic region (2820–2990 cm^{-1}) exhibit high loadings, while for PC2, the long-chain region (833–912 cm^{-1}) and the region between 1100 and 1330 cm^{-1} as most critical.

Both PC1 and PC2 were found to be crucial for understanding laboratory aging processes and for making comparisons between laboratory and field-aged samples. Consequently, the spectral regions with consistently high loadings across both principal components —734–912 cm^{-1}, 1100–1330 cm^{-1}, and 2820–2990 cm^{-1} —were selected for further deconvolution and DTW analysis. These regions have also been recognized as significant in previous studies [47].

To quantify the similarity between field-aged and laboratory-aged

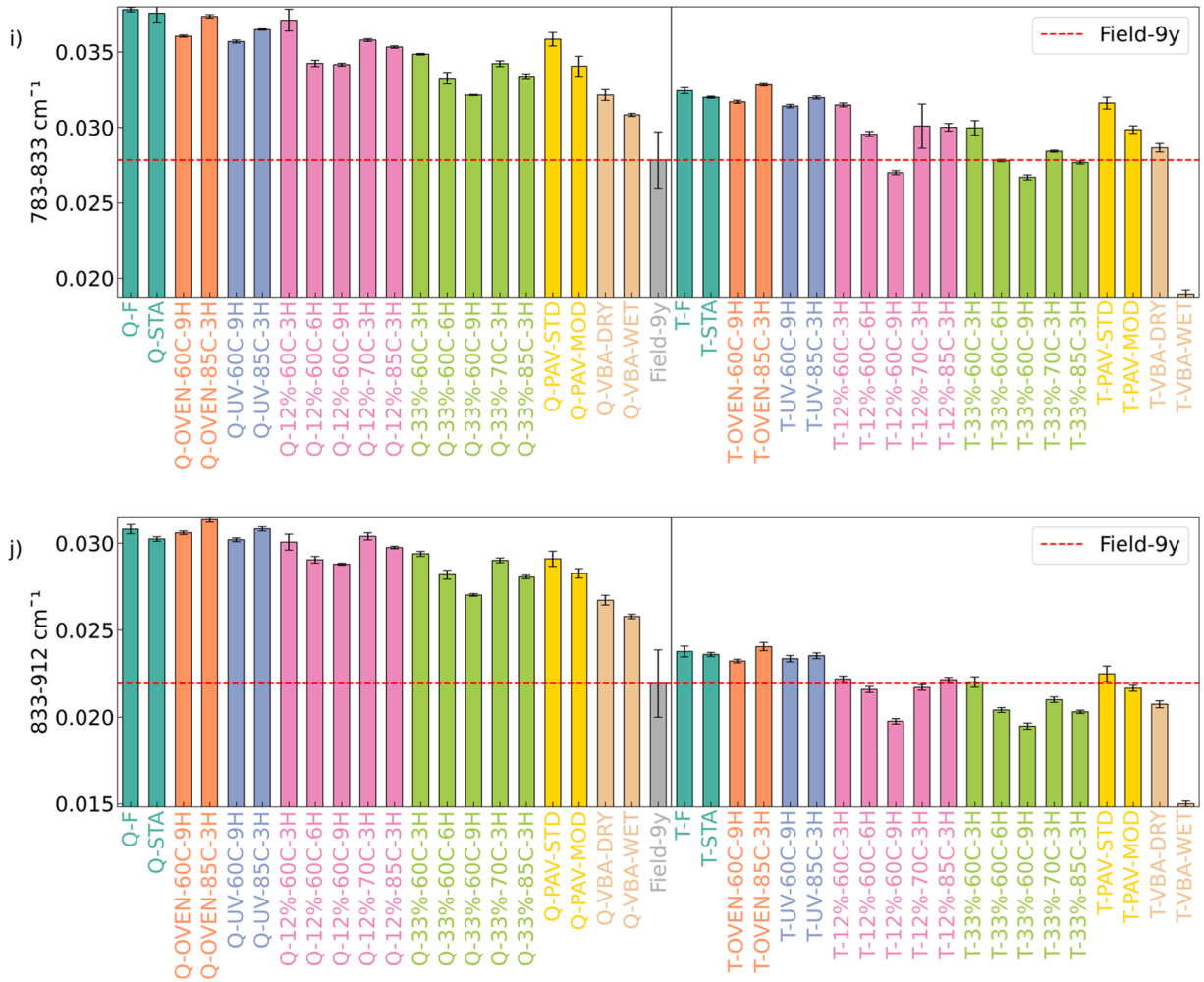

Fig. 2. (*continued*).

samples, Euclidean distance was calculated using the two principal components obtained from PCA analysis of FTIR indices, as plotted in Fig. 4. Field-9y was used as the reference group. The distances between this reference and the laboratory-aged samples were computed. A smaller distance indicates a closer aging level, with exact distance values in an ascending order presented in Table 2S. The results indicate that Field-9y is most closely matched with Q-VBA-WET, followed by Q-33 %-60C-9H, Q-VBA-DRY, Q-33 %-85C-3H, Q-PAV-MOD, and Q-33 %-60C-6H. This suggests that the UPA aging methods are among the closest to approximate field conditions in terms of chemical components.

4.4. Comparison between field and laboratory aging using spectral deconvolution and DTW

To further analyse aged-caused chemical changes and to evaluate the similarities between various aging protocols, FTIR spectral deconvolution was performed, focusing on key regions identified by the PCA loadings in Fig. 5. The deconvoluted spectra of Field-9y are shown in Fig. 6a-d, covering the regions of 680–900 cm^{-1} (6 peaks), 900–1550 cm^{-1} (16 peaks), 1550–1750 cm^{-1} (5 peaks), and 2600–3100 cm^{-1} (5 peaks). Detailed information on the number of deconvoluted peaks, their positions, heights, and areas for all samples, along with visual representations of the deconvoluted spectra, are provided in the supporting information.

The exact deconvoluted peak positions and their corresponding functional groups can be found in Table 3S. The region of 680–900 cm^{-1} primarily contains bands associated with out-of-plane (δo-p) C–H bending in aromatic rings and the bending vibrations of secondary amides and alkyl side chains. The reduction in this region (Fig. 2g-j) can be attributed to the oxidative degradation of aromatic hydrocarbons and the breakdown of secondary amides and alkyl side chains. During oxidative aging, the C–H groups adjacent to the aromatic ring in bitumen may be substituted by polar oxidized groups, leading to a reduction in the intensity of aromatic C–H bending vibrations. Additionally, secondary amides might be cleaved, leading to a reduction in the N–H bending intensity. Alkyl side chains, particularly those with four or more carbons, can undergo oxidation, resulting in shorter chains or the formation of oxidized products, thereby decreasing the C–CH_2 rocking vibrations.

The 900–1550 cm^{-1} region is rich in functional groups associated with C-H bending, C-O stretching in ethers, esters, and phenols, as well as sulfoxide and aromatic C═C stretching vibrations. The increase in the indices within this region can be explained by the formation of oxidation products. Aromatic rings in bitumen can be functionalized through oxidation, leading to the formation of oxygen-containing functional groups such as ethers, esters, phenols, and sulfoxides. These groups contribute to the increase in C-O stretching (1069–1187 cm^{-1}) and S═O stretching (1031 cm^{-1}). Additionally, the formation of aromatic sulfoxides and the introduction of hydroxyl or alkoxy groups into the aromatic rings result in increased bending and stretching vibrations characteristic of these groups. The C-H bending modes associated with the aromatic ring structures also increase as new substituted aromatics are formed.

The 1550–1750 cm^{-1} region is primarily characterized by the stretching vibrations of carbonyl groups (C═O) and aromatic C═C

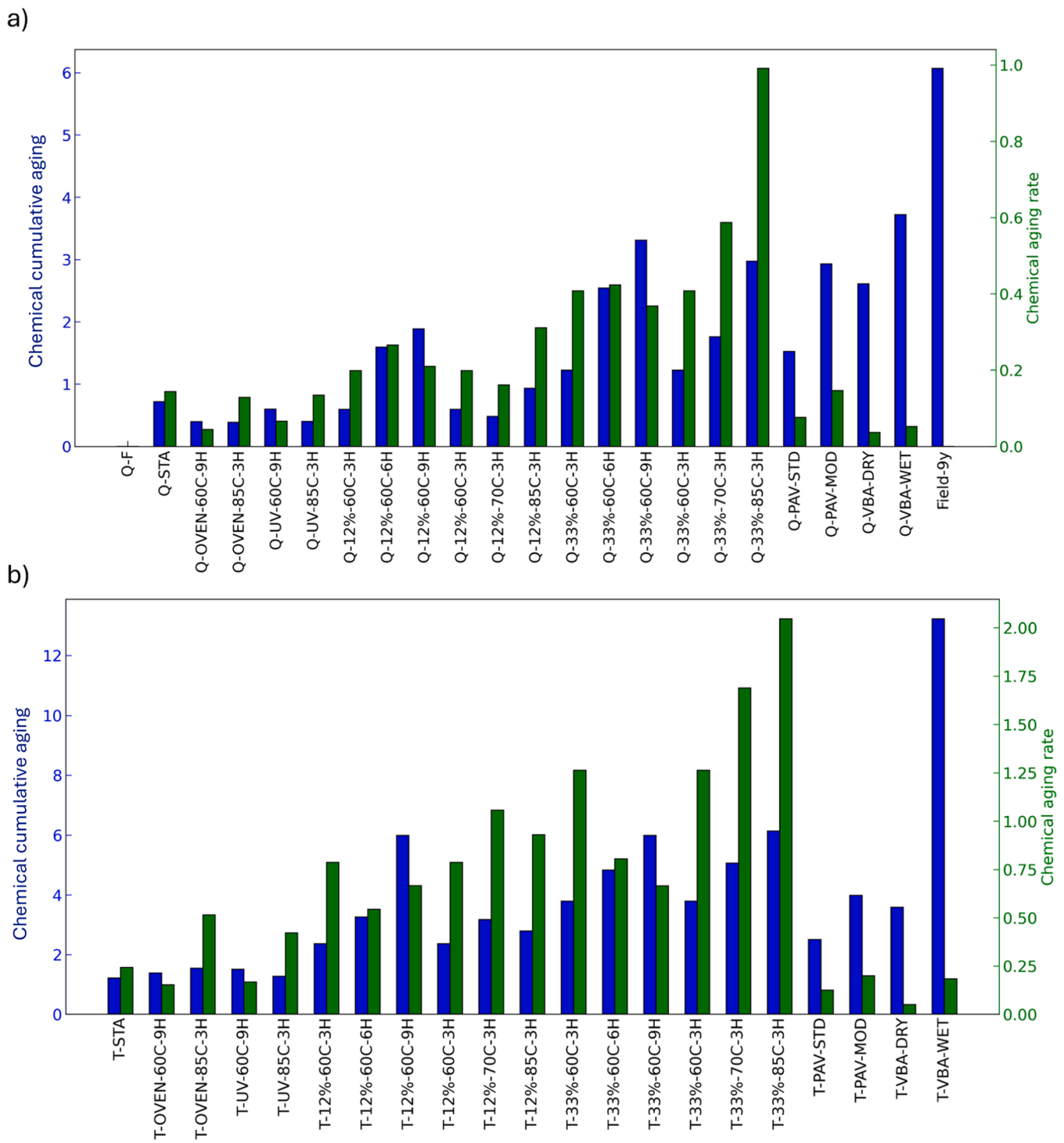

Fig. 3. Cumulative aging and aging rate of a) Q binder and b) T binder calculated based on chemical properties.

bonds. The increase in the index for this region suggests a growth in oxygenated functional groups, such as esters, carboxylic acids, and amides, which are products of oxidative aging. The presence of the carbonyl stretching vibrations is linked to the formation of conjugated systems, including ketones and carboxyl compounds, as well as the evolution of aromatic groups in the material. These carbonyl-related bands indicate the ongoing oxidation and breakdown of aliphatic chains, leading to the incorporation of oxygenated species. Additionally, the increase in aromatic C═C stretching, and the reduction of aliphatic components further emphasize the aging process, where aromatic condensation and oxidation contribute to the changes in the chemical composition of the material.

The 2600–3100 cm^{-1} region is dominated by C-H stretching vibrations of methyl and methylene groups. The decreased absorbance in this region is likely due to oxidative degradation processes such as the breaking of C-H bonds in aliphatic chains, leading to the formation of carbonyl-containing compounds (e.g., aldehydes, ketones, and carboxylic acids) or the complete cleavage of these chains, leading to the loss of methyl and methylene groups. This process is consistent with the general understanding of bitumen aging, where the material becomes more oxygenated, leading to a decrease in the intensity of aliphatic C-H stretches. As a summary, oxidative aging results in the depletion of

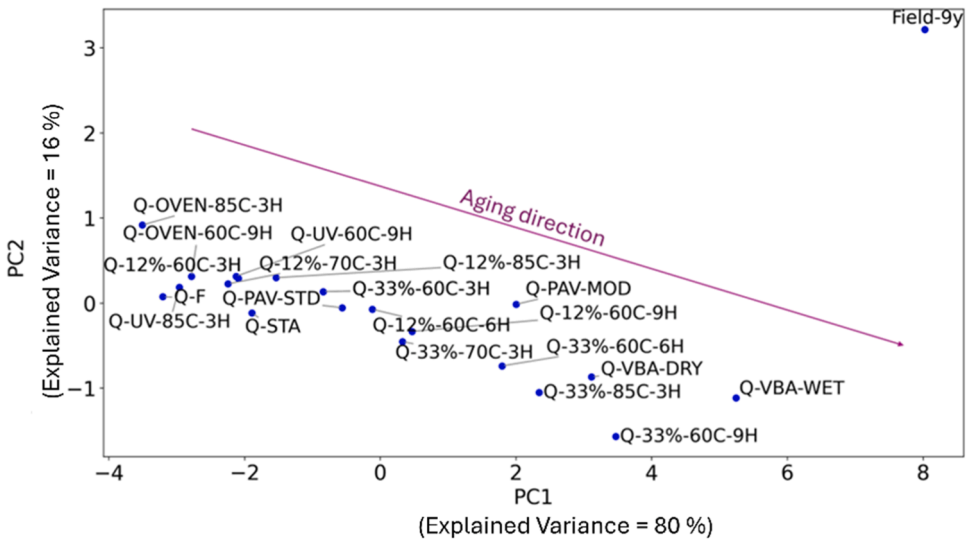

Fig. 4. PCA plot based on FTIR indices for Q binder in different aging states including, fresh, short-term aged, long-term aged of all conditions for OVEN, UV, UPA, PAV-STD, PAV-MOD, VBA-DRY, VBA-WET, and a 9-year field-aged sample.

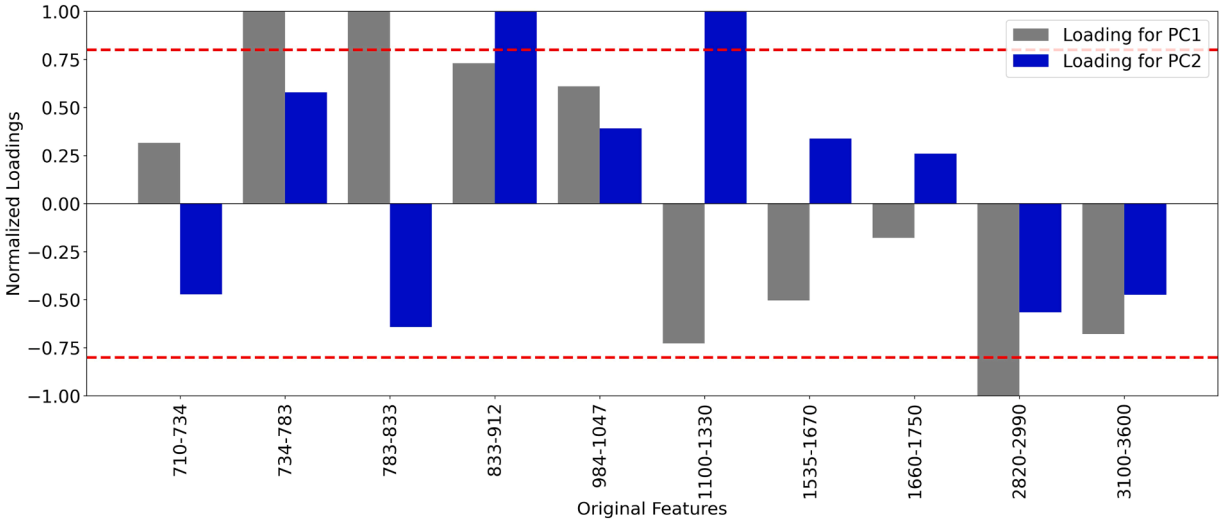

Fig. 5. Loading of all features (FTIR indices) on PC1 and PC2, for Q binders. A threshold of ± 0.8 was applied to determine the significance of these loadings.

aliphatic and hydrocarbon structures, the formation of oxygenated and sulfur-containing species, and increased aromatic condensation.

The peak positions within these regions are specific to each sample. This shift reduces the accuracy of Euclidean distance for comparing aging similarity. To achieve a more precise chemical similarity comparison without being affected by the shifts of peaks positions, the dynamic time warping (DTW) method was employed. DTW realigns the deconvoluted peak positions, allowing for comparison between samples with shifted peaks due to aging. Only the six samples previously identified as closest to Field-9y by the Euclidean distance analysis (based on the two principal components obtained from PCA analysis, Table 2S) were included. Samples that did not rank in the top six based on Euclidean distance had a limited likelihood of exhibiting the highest similarity using the DTW method.

Table 4 presents the alignment cost (peak position shifts) and Euclidean distance of peak areas corresponding to the aligned peak positions of the six samples. The alignment cost indicates the extent to which peak positions need to be adjusted to match the reference spectrum (Field-9y), with lower alignment costs suggesting a more similar peak alignment to Field-9y, and peak positions that better resemble those observed in the field sample. Similarly, lower Euclidean distances of peak areas indicate a closer chemical resemblance to the field sample. Results showed the sample 33 %-60C-6H as the closest to the field-aged sample based on peak position shifts, with 33 %-60C-9H being the least similar. When the Euclidean distances of peak areas were considered (Table 4), 33 %-60C-6H remained the closest, while the ranking of other samples changed. This ranking difference underscores the importance of both peak position and peak area in determining the similarity between samples. It is worth noting that, based on both peak positions and peak areas, the sample 33 %-60C-6H shows the closest resemblance to the field sample, with a significantly lower Euclidean distance compared to other samples. Interestingly, considering both peak positions and peak areas suggests that incorporating ROS molecules at 60 °C for 6 h into aging conditions brings the chemical aging process closer to field aging compared to other aging conditions. This indicates that UPA aging most effectively replicates field aging, demonstrating both a high degree of chemical similarity and an accelerated aging rate, as evidenced by aging rate analyses. These findings establish UPA as a laboratory aging method that is both efficient and accurate.

The discrepancy in aging order (using field sample as the reference)

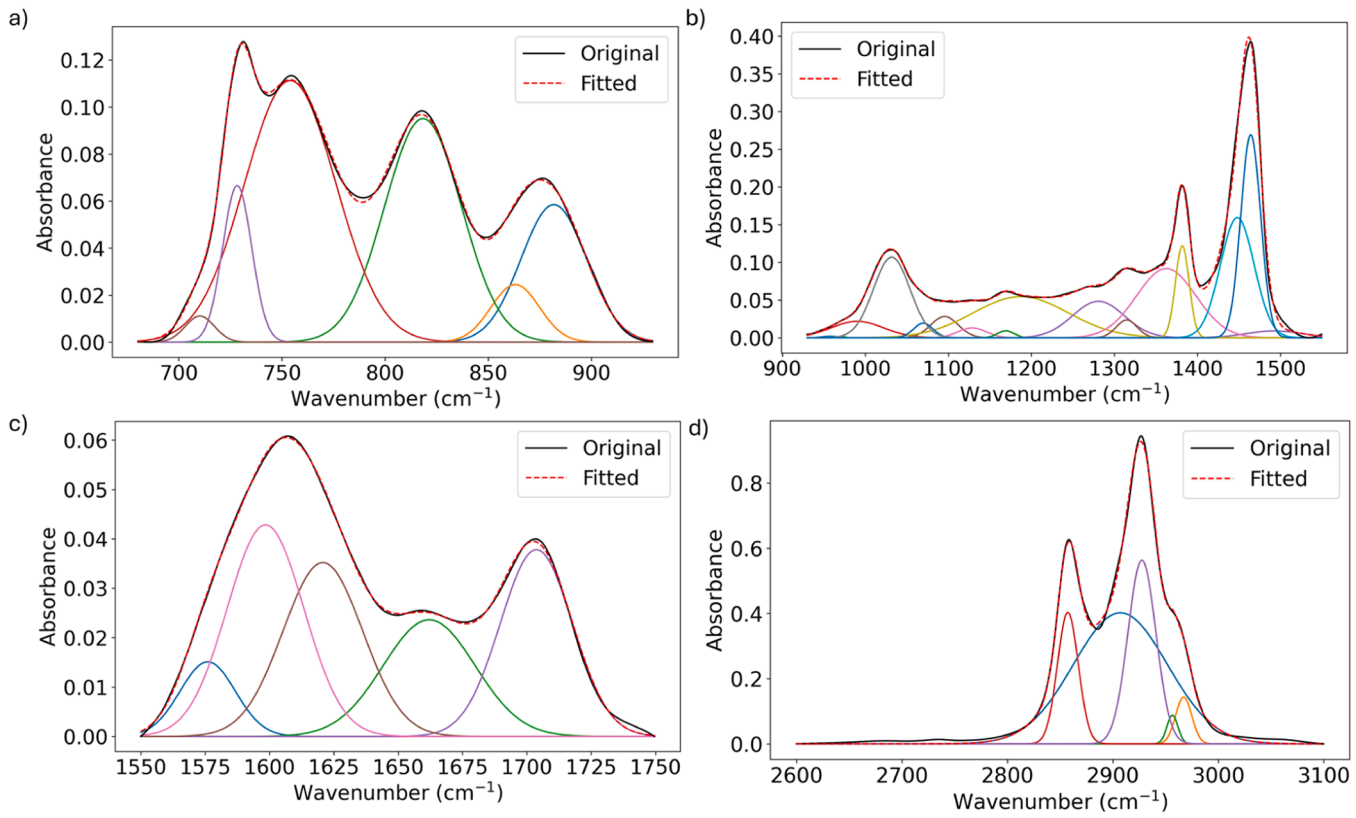

Fig. 6. FTIR spectrum of the 9-year field-aged sample deconvoluted separately in different regions: a) 680–900 cm^{-1}, b) 900–1550 cm^{-1}, 1550–1750 cm^{-1}, and c) 2600–3100 cm^{-1}.

Table 4
Alignment cost and Euclidean distance of peak areas corresponding to the aligned peak positions of the six samples closest to Field-9y based on PCA and Euclidean distance analysis (Table 2S).

Sample	Peak position shifts/ DTW Alignment cost (cm^{-1})	Euclidean distance of peak areas corresponds to aligned peak positions
Field−9y (Reference)	0	0
Q−33 %-60C-6H	288.03	12.68
Q-PAV-MOD	291.85	32.58
Q-VBA-WET	333.83	32.95
Q-VBA-DRY	345.71	32.77
Q−33 %-85C-3H	369.72	33.49
Q−33 %-60C-9H	381.35	32.79

between Euclidean distance calculations from PCA (linear combination of FTIR indices) and deconvolution likely results from their differing focus. PCA based on FTIR indices captures the cumulative effect of multiple overlapping bands, potentially masking subtle changes, whereas deconvolution isolates individual peaks, highlighting specific chemical changes that might be more sensitive to aging. The differences in how these methods handle spectral overlap, sensitivity to minor chemical changes, and the contributions of various functional groups, as well as potential artifacts from the deconvolution process, can lead to variations in the observed aging order.

4.5. Aging effects on rheological properties

To further compare the various aging protocols, rheological properties were utilized to complement and verify the chemical analysis results. Due to the large number of conditioned samples (22 for each binder), only those with the highest chemical aging rates were included to maintain plot clarity. For both Q and T binders, the selected samples were fresh, STA, OVEN/UV-85C-3H, 12/33 %-60C-9H, 12/33 %-85C-3H, PAV-STD, PAV-MOD, VBA-DRY, VBA-WET, and field-aged samples.

The master curves for Q and T binders are shown in Fig. 7a and b, respectively. The G* master curve of various lab-aged samples show increasing stiffness. This increased stiffness is primarily driven by polymerization and oxidative crosslinking reactions, which increase molecular weight and reduce molecular mobility, leading to stiffening of the binder. As oxidation progresses, the formation of polar functional groups (e.g., carbonyl and sulfoxide) enhances intermolecular interactions, promoting the development of a more rigid network. For all aging protocols, a similar G* master curve shape like that of the field-aged sample was observed, expect the VBA-aged samples, which deviated slightly to lower G* values at high frequencies. The slight deviation of the VBA-aged samples from other aging methods suggests that this protocol might introduce specific chemical modifications that differ from conventional aging mechanisms. For δ master curve, the field-aged sample showed the steepest slope, indicating more rapid hardening from low to high frequencies, while all other lab-aged samples had gentler slopes, demonstrating slower changes. This suggests that field aging leads to a broader distribution of molecular structures, resulting in a more heterogeneous network that hardens more significantly across the frequency spectrum. The laboratory aging protocols, although effective, do not fully replicate the complex interactions occurring over long-term field exposure. Furthermore, compared to complex modulus, the phase angle exhibits a more significant variation in both shape and magnitude across different aging protocols. This suggests that the phase angle master curve is more sensitive to aging and can better differentiate aging conditions.

For the Q binder, the G* and δ master curves of the OVEN/UV-85C-

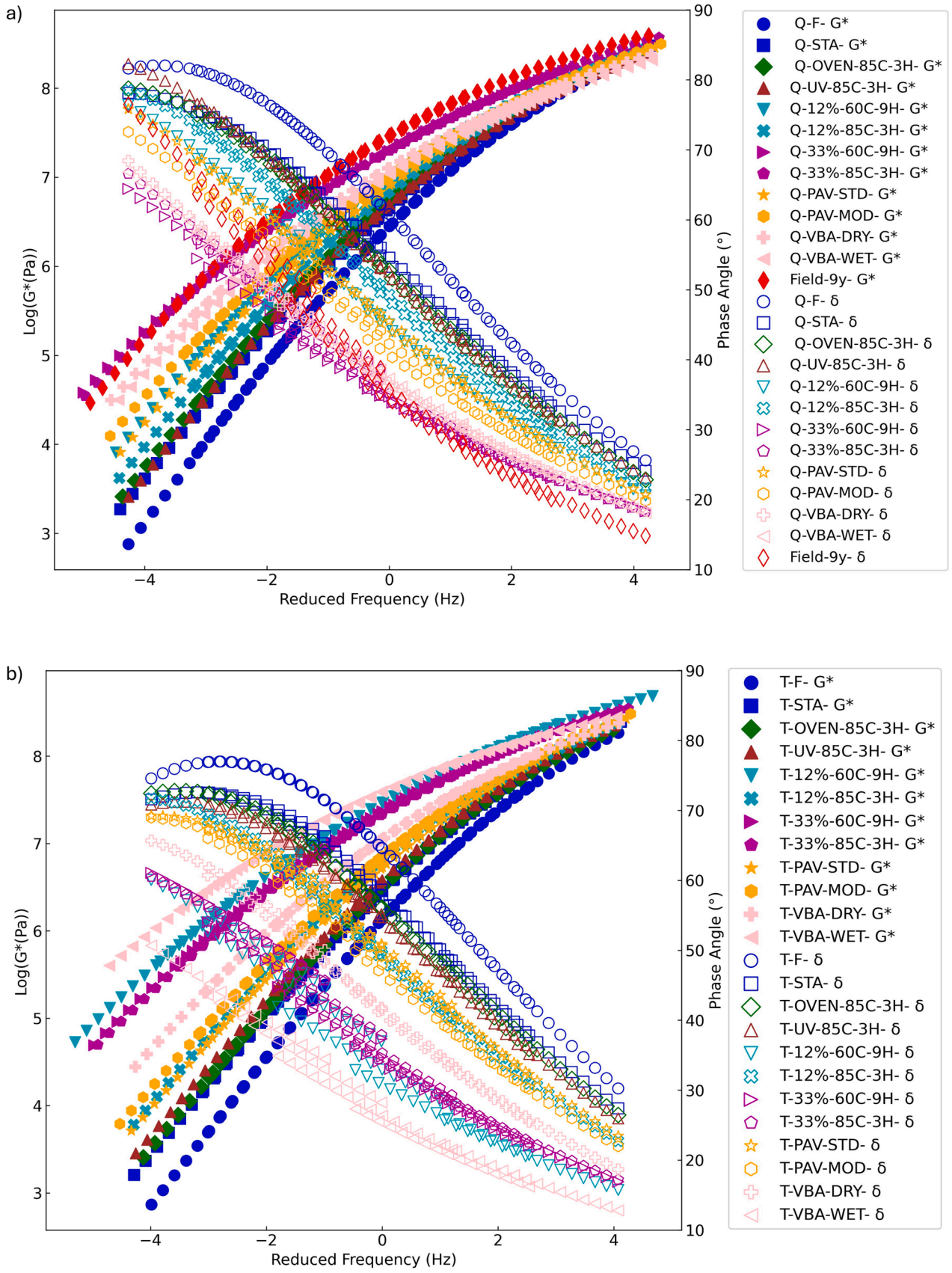

Fig. 7. Master curves (at 20 °C) at different aging conditions of a) Q binder, and b) T binder. In Figure a, the field sample's master curves are plotted in red.

3H samples overlapped with the STA sample, indicating minimal aging. This suggests that the thermal and UV exposure for 3 h at 85°C is not sufficient to induce significant oxidative aging, as observed in the chemical analysis. The lack of substantial changes in G* and δ implies that this aging condition does not generate enough oxidative species to alter the binder's rheological response. The PAV-STD aged samples displayed slightly less aging compared to the PAV-MOD samples for both Q and T binders. The VBA-WET and VBA-DRY samples behaved similarly for the Q binder. For the T binder, the T-12 %-60C-9H and T-VBA-WET samples exhibited extreme aging, consistent with FTIR results. This highlights the influence of binder composition on aging susceptibility.

For UPA aged samples with 12 % H_2O_2, those aged at 85°C for 3 h exhibited less aging than those aged at 60°C for 9 h. Samples aged with 33 % H_2O_2 showed similar master curves for both aging conditions. This indicates that, at lower concentrations (12 %), longer exposure at a moderate temperature (60°C for 9 h) results in more pronounced aging than a shorter duration at a higher temperature (85°C for 3 h). In contrast, at a higher concentration (33 %), the impact of temperature and time appears to be less significant, suggesting that oxidation is predominantly driven by the H_2O_2 concentration rather than thermal effects.

Comparison with 9 years of field aging revealed that UPA aged samples, Q-33 %-60C-9H and Q-33 %-85C-3H, closely matched the G* master curve and had minimal deviation in the δ master curve, indicating the suitability of these UPA protocols for rapid simulation of field aging. This provides strong evidence that the UPA method, particularly with 33 % H_2O_2, effectively replicates the long-term oxidative aging observed in field conditions.

Furthermore, two critical parameters—crossover frequency (CR-Fr) and crossover complex modulus (CR-CM)—were calculated. These crossover values represent significant points on the viscoelastic spectrum that are independent of test frequency and temperature. Previous studies have shown that lower CR-Fr values in aged binders correlate with higher molecular mass, longer relaxation times, and higher softening points [48,49]. Lower CR-CM values indicate higher polydispersity, reflecting a broader distribution of molecular masses. A higher crossover frequency suggests more elastic behaviour at higher frequencies, contributing to enhanced resistance against permanent deformation or rutting, especially under repeated traffic loading. A higher crossover modulus indicates increased stiffness at the crossover frequency, further improving resistance to rutting.

Fig. 8 shows the CR-Fr vs. CR-CM plot for Q binders. An aging trend toward lower CR-Fr and CR-CM values is observed. Samples aged by OVEN, UV, and 12 % UPA exhibited similar CR-Fr and CR-CM values. Increasing the aging temperature resulted in lower crossover values, and adding humidity further decreased these values for PAV-aged samples. This suggests that oxidation-driven molecular weight increases, and structural modifications contribute to reduced crossover values, with temperature playing a significant role in accelerating aging. However, for VBA-aged samples, humidity appears to have a minimal impact, potentially indicating that this protocol primarily induces oxidation through mechanisms less dependent on moisture.

Comparing lab-aged samples with field-aged ones, two samples—Q-33 %-60C-9H and Q-33 %-85C-3H—were found to be closest to the field samples. This observation is consistent with findings from master curve analyses, strengthens the reliability of these protocols as effective field-aging alternates.

For the T binder, similar aging direction was observed towards lower crossover values (Fig. 9). Similar to Q binder, OVEN and UV-aged samples sharing similar crossover values. PAV aged samples are located lower than oven and UV aged samples. Adding humidity increased aging for both PAV and VBA aged samples. Moreover, PAV aged samples with or without humidity are located between oven and UV aged samples with high crossover values and UPA samples with lower crossover values showing that T binder is sensitive to the presence of ROS during aging. This again emphasizes the role of ROS in modifying the T binder's molecular structure, with UPA samples exhibiting the most significant oxidation effects. The lower crossover values for UPA-aged samples indicate substantial molecular restructuring, consistent with advanced oxidative aging.

The sample T-12 %-70C-3H is located higher than fresh sample showing fresh condition of binder. further repetitions and testing are needed to assure the location of this sample. Other UPA samples moved towards lower crossover values by increasing temperature or time. Similar to the observation from master curves and FTIR data, T-VBA-WET and T-12 %-60C-9H are extremely aged. Interestingly, considering standard deviations, all the 33 % UPA aged samples are located in the same range of crossover values indicating stronger effect of high concentration H2O2 than temperature or time of aging for T binder. This suggests that for T binder, oxidative aging is primarily driven by H_2O_2 concentration rather than temperature or exposure duration.

4.6. *Cumulative aging and aging rate based on rheological properties*

Next, the cumulative aging (CA) and aging rate (AR) were calculated using rheological properties (Eqs. 10 and 12). Fig. 10 a) and Fig. 10 b)

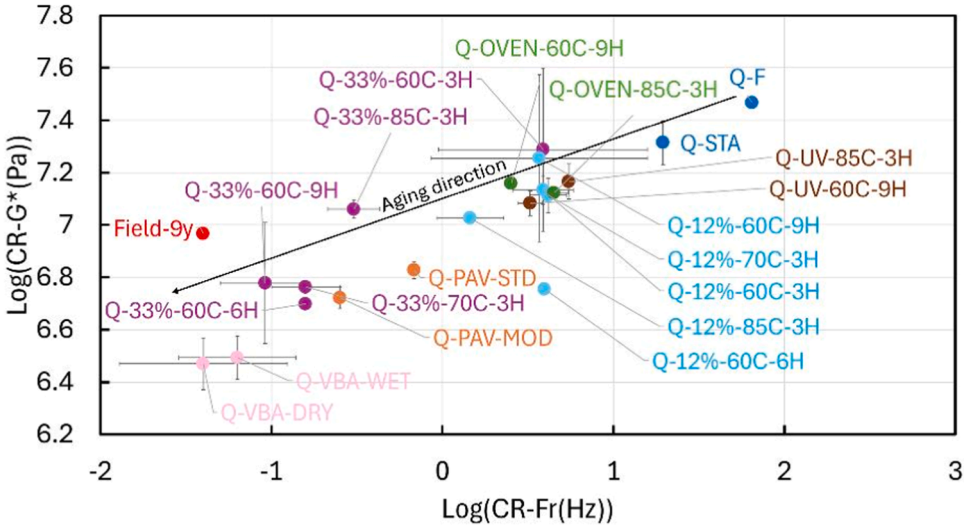

Fig. 8. Crossover complex modulus versus crossover frequency of Q binder samples, including fresh, short-term aged, long-term aged samples and a 9-year field-aged sample.

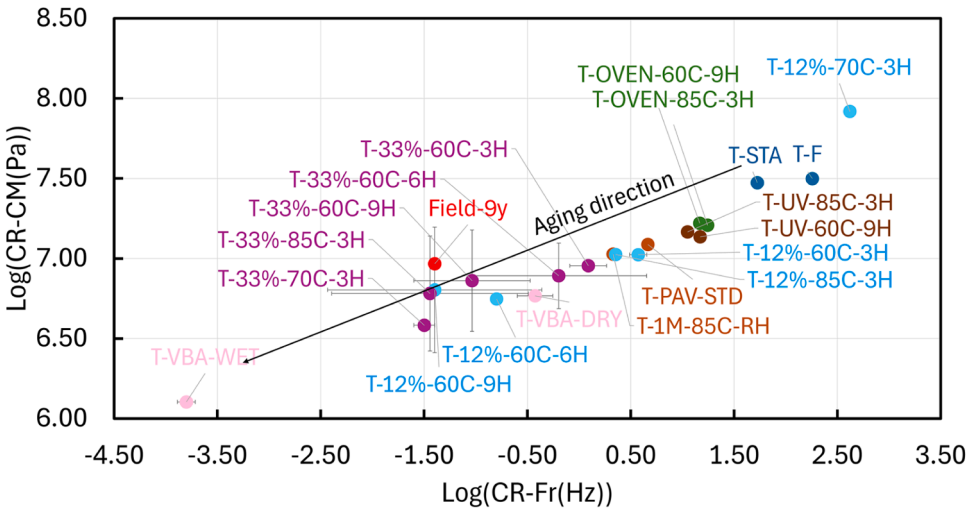

Fig. 9. Crossover complex modulus versus crossover frequency of T binder samples, including fresh, short-term aged, long-term aged samples.

present the CA and AR values for Q and T binders, respectively. For the Q binder, UPA aged samples Q-33 %-60C-9H and Q-33 %-85C-3H were the most aged in the lab, CA values close to the 9-year field-aged sample. The Q-33 %-85C-3H sample also exhibited the largest AR value. The higher rheological aging rate in UPA-aged samples, particularly Q-33 %-85C-3H, is due to the combined effects of ROS-induced oxidation and elevated temperature, which together accelerate molecular restructuring. For the T binder, the T-12 %-60C-9H and T-VBA-WET samples showed the CA values, but their ARs were much slower than that of the T-33 %-85C-3H sample, which had the highest aging rate. The divergences between the effects of various aging conditions on rheological behaviour of Q and T binders, as also observed in the chemical properties, result from compositional differences, such as variations in asphaltene content, which influence the extent and rate of rheological changes under different oxidative conditions.

4.7. Chemo-rheological analysis

To further discuss various aging protocols by combining chemical and rheological properties, we first analysed the chemo-rheological correlations and then compared the efficiency and accuracy of those protocols combining results from both aspects.

The linear relationships between key chemical and rheological parameters were analysed using the Pearson correlation analysis, as show in Fig. 11. High Pearson values were observed between rheological properties and some chemical parameters, indicating strong relationships between chemical changes and rheological properties due to aging. The high negative correlation (-0.70) between 1100–1330 cm^{-1} and CR-Fr suggests that oxidation-induced polar functional groups contribute to increased stiffness. The inverse correlation of 1535–1670 cm^{-1} with CR-Fr (-0.81) reflects that the formation of condensed aromatic structures results in increased stiffness. Except this, the generally low correlations between most FTIR indices and rheological parameters indicate that a peak does not represent fully binder chemical properties and thus cannot be correlated well with rheological properties. Therefore, a combination of multiple peaks is necessary for a more comprehensive chemo-rheological analysis.

To determine the optimized aging protocol, both chemical and rheological analysis based on the PCA, Euclidean distance, cumulative aging and aging rate indices, and integrated deconvolution and DTW were used. From a chemical perspective, aging with 33 % H_2O_2 at 60°C for 6 h was found to closely replicate the characteristics of field-aged samples. Subsequently, the condition of 33 % H_2O_2 at 60°C for 9 h emerged as the closest and fastest alternative for chemical replication. Rheologically, the aging conditions of 33 % H_2O_2 at 85°C for 3 h or 60°C for 9 h were found to closely align with the field-aged reference samples. By combining the results of chemical analysis with rheological assessments, it can be concluded that a 33 % H_2O_2 solution at 85°C for 3 h, or at 60°C for 6–9 h, provides an optimized protocol. This condition effectively mimics both the chemical and rheological properties of field-aged materials while offering a faster alternative to conventional aging methods, such as PAV or VBA. As a result, this protocol is recommended for future studies.

4.8. UPA aging mechanisms

The probable mechanism of accelerated oxidation of UPA are summarized as follows:

In initiation phase, the exposure of hydrogen peroxide to UV light leads to its photolysis, producing hydroxyl radicals (HO•) as described in reaction (9). This reaction is the rate-limiting reaction, since the other reactions' rates (reactions 10–20) are way higher than Eq. 8.

$$H_2O_2+h\nu \rightarrow 2HO\bullet \quad (9)$$

Given the similarity to field aging where oxidative degradation is a key process, the formation of HO• can be seen as analogous to the initiation of oxidation in the field, where atmospheric oxygen and environmental factors contribute to the formation of ROS such as HO•.

In propagation phase, hydroxyl radicals react with H_2O_2 to form perhydroxy radicals ($HO_2\bullet$) and water (Eq. 10). $HO_2\bullet$ further reacts with H_2O_2 to regenerate HO•, producing water and oxygen (Eq. 11).

$$H_2O_2+HO\bullet \rightarrow HO_2\bullet+H_2O \quad (10)$$

$$H_2O_2+HO_2\bullet \rightarrow HO\bullet+H_2O+O_2 \quad (11)$$

Binder aging happens at this stage when hydroxyl radicals abstract hydrogen from binder (RH), forming alkyl radicals (R•) (Eq. 12). Then, alkyl radicals react with oxygen to form peroxyl radicals ($RO_2\bullet$), and peroxyl radicals react with more binder, forming hydroperoxides (ROOH) and regenerating alkyl radicals (Eqs. 13 and 14).

$$RH+HO\bullet \rightarrow R\bullet+H_2O \quad (12)$$

$$R\bullet+O2 \rightarrow RO_2\bullet \quad (13)$$

$$RO_2\bullet+RH \rightarrow ROOH+R\bullet \quad (14)$$

Moreover, hydroperoxides (ROOH) react with sulfides in the binder to form sulfoxides (Eq. 15).

$$ROOH+RSR \rightarrow ROH+RSOR \quad (15)$$

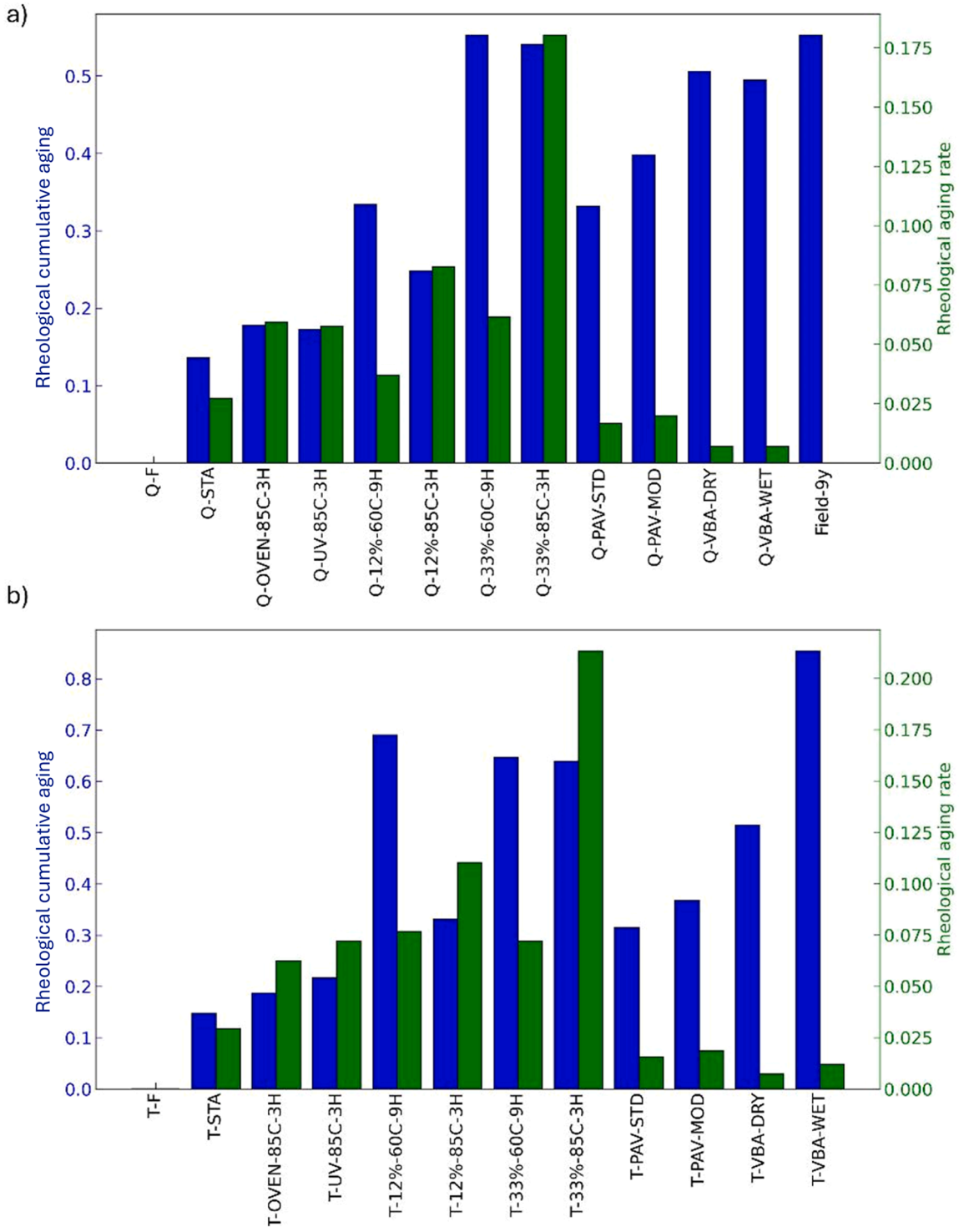

Fig. 10. Rheological changes due to aging and aging rate of a) Q binder, and b) T binder.

Furthermore, hydroperoxides decompose, especially at higher temperatures, to form free radicals which then react with benzylic carbons and lead to ketone formation (Eqs. 16 and 17).

$$ROOH \rightarrow RO\bullet + HO\bullet \quad (16)$$

$$RO\bullet \rightarrow R{=}O \quad (17)$$

The elevated temperature (85°C) enhances the reactivity of these radicals and the overall rate of chemical reactions. The formation of these oxidation products is consistent with the increase in C-O stretching and sulfoxide vibrations observed in the field-aged sample. The formation of ketones corresponds to the carbonyl-containing compounds observed in the field-aged sample, such as aldehydes, ketones, and carboxylic acids. The reduction in aliphatic C-H stretches in the 2600–3100 cm^{-1} region in field-aged samples suggests similar oxidative cleavage of C-H bonds leading to carbonyl formation.

While termination reactions by radical recombination (Eqs. 18–20) leads to the formation of less reactive species eventually reduce the concentration of radicals.

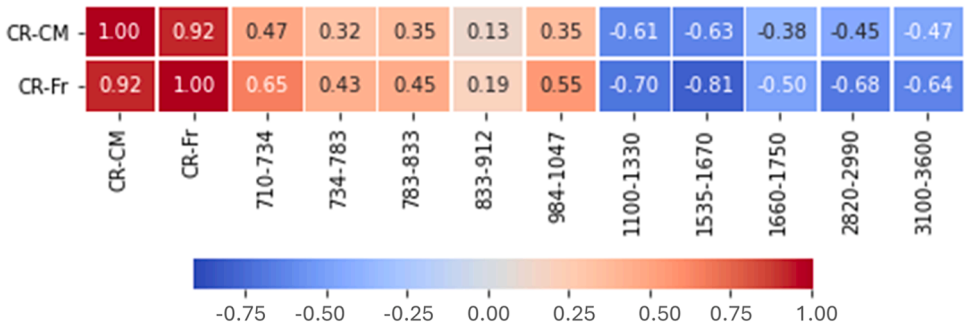

Fig. 11. Pearson correlation heatmap showing the relationships between spectral regions and rheological parameters (CR-CM and CR-Fr).

$$2HO\bullet \rightarrow H_2O_2 \quad (18)$$

$$2HO_2\bullet \rightarrow H_2O_2 + O_2 \quad (19)$$

$$HO\bullet + HO_2\bullet \rightarrow H_2O + O_2 \quad (20)$$

The field aging process involves the oxidative degradation of aromatic hydrocarbons, breakdown of secondary amides, and shortening of alkyl side chains, which are paralleled by the reactions in the UPA protocol. The UPA method reproduces a highly oxidative environment that mirrors the natural aging processes, and the complex interplay of photochemical, thermal, and oxidative processes makes it more representative of field aging compared to other laboratory methods that may lack one or more of these critical factors. The hydroxyl and perhydroxy radicals generated through the photolysis and subsequent reactions of H_2O_2 rapidly attack the binder, leading to the formation of hydroperoxides, sulfoxides, and ketones, similar to field aging. By focusing on these detailed oxidative mechanisms, the UPA protocol can be better understood as an accelerated aging process that replicates the primary chemical transformations occurring in field-aged bitumen.

5. Conclusion

This study introduced a novel bitumen aging protocol, termed UPA, which combines UV exposure and H_2O_2 to accelerate aging while closely replicating field conditions. The effectiveness of UPA was evaluated by comparing the chemical and rheological properties of UPA-aged samples with those aged using conventional aging methods (PAV, VBA, UV, and oven aging) and a nine-year field-aged sample.

FTIR results showed that UPA led to significant oxidation, increasing carbonyl, sulfoxide, and hydroxyl functional groups while degrading aliphatic chains. Among all tested aging protocols, the UPA aging with 33 % H_2O_2 at 85°C for 3 h or at 60°C for 6–9 h provided the closest match to field aging in both chemical and rheological aspects. The UPA also presents a higher aging rate compared to the PAV and VBA methods, attributed to the hydroxyl radicals generated from the photodecomposition of H_2O_2 under UV light.

This study also introduced robust methods for accurately comparing lab- and field-aged samples, including FTIR-based PCA for visualizing sample similarities, Euclidean distance for qualifying differences, integrated FTIR spectral deconvolution and DTW alignment to enable precise comparison unaffected by peak shifts, and rheological parameter analysis. These methods improve the assessment of aging protocols and provide a structured approach for comparing binder samples measured by FTIR and DSR, focusing on identifying the most critical cases.

Future research will be focused on exploring the effects of UPA on SARA fractions and binder microstructure, as well as its application to mastic and mixture samples to refine the aging process for broader use in pavement engineering. Moreover, additional field samples will be evaluated to validate the feasibility of this method for different field aging durations. Furthermore, additional aging factors, including repeated loads and water damage, will be evaluated to provide a more comprehensive assessment of the aging process.

CRediT authorship contribution statement

Khalighi Sadaf: Writing – review & editing, Writing – original draft, Visualization, Validation, Methodology, Investigation, Formal analysis, Conceptualization. **Ma Lili:** Writing – review & editing. **Varveri Aikaterini:** Writing – review & editing, Supervision, Funding acquisition.

Declaration of Competing Interest

The authors declare that they have no known competing financial interests or personal relationships that could have appeared to influence the work reported in this paper.

Acknowledgment

This paper/article is created under the research program Knowledge-based Pavement engineering (KPE, funded by Rijkswaterstaat, contract number = 31164321). KPE is a cooperation between Rijkswaterstaat, TNO and TU Delft in which scientific and applied knowledge is gained about asphalt pavements and which contributes to the aim of Rijkswaterstaat to be completely climate neutral and to work according to the circular principle by 2030. The opinions expressed in this paper is solely from the authors.

Appendix A. Supporting information

Supplementary data associated with this article can be found in the online version at doi:10.1016/j.conbuildmat.2025.141272.

Data Availability

Data will be made available on request.

References

[1] S. Salehi, et al., Sustainable pavement construction: a systematic literature review of environmental and economic analysis of recycled materials, J. Clean. Prod. 313 (2021) 127936.
[2] L. Lyu, et al., Aging evolution and sustainability implications of crumb rubberized asphalt binder: a state-of-the-art, J. Clean. Prod. 434 (2024) 140202.
[3] M. Ahmad, et al., Aging characterization of asphalt binders through multi-aspect analyses: a critical review, Fuel 376 (2024) 132679.
[4] R. Tauste, et al., Understanding the bitumen ageing phenomenon: a review, Constr. Build. Mater. 192 (2018) 593–609.
[5] G.D. Airey, State of the art report on ageing test methods for bituminous pavement materials, Int. J. Pavement Eng. 4 (3) (2003) 165–176.
[6] B. Hofko, M. Hospodka, Rolling thin film oven test and pressure aging vessel conditioning parameters: effect on viscoelastic behavior and binder performance grade, Transp. Res. Rec. 2574 (1) (2016) 111–116.
[7] A. Koyun, et al., Rheological, spectroscopic and microscopic assessment of asphalt binder ageing, Road. Mater. Pavement Des. 23 (1) (2022) 80–97.

[8] S.S. Nagabhushanarao, A. Vijayakumar, Chemical and rheological characteristics of accelerate aged asphalt binders using rolling thin film oven, Constr. Build. Mater. 272 (2021) 121995.
[9] EN 12607-1, C.. 12607-1: Bitumen and Bituminous Binders—Determination of the Resistance to Hardening under Influence of Heat and Air—Part 1: RTFOT Method, European Committee for Standardization, Brussels, Belgium, 2014.
[10] EN 14769, C, Bitumen and Bituminous Binders—Accelerated Long-Term Ageing Conditioning by a Pressure Ageing Vessel (PAV), European Committee for Standardization, Brussels, Belgium, 2012, p. 14769. EN 14769,.
[11] J.C. Petersen, A review of the fundamentals of asphalt oxidation: chemical, physicochemical, physical property, and durability relationships, Transp. Res. Circ. (E-C140) (2009).
[12] H. Ezzat, et al., Comparative analysis of non-standardised aging methods for asphalt binder against standard laboratory aging and natural field aging, Int. J. Pavement Eng. 25 (1) (2024) 2414089.
[13] B.T. Smith, et al., Comparing laboratory pressure aging vessel conditioning to field aging of asphalt binder within compacted mixtures, J. Mater. Civ. Eng. 31 (11) (2019) 04019271.
[14] Lu, X., Y. Talon, and P. Redelius. Aging of bituminous binders–laboratory tests and field data. in Proceedings of the 4th Eurasphalt & Eurobitume Congress, Copenhagen. 2008.
[15] R. Jing, et al., Laboratory and field aging effect on bitumen chemistry and rheology in porous asphalt mixture, Transp. Res. Rec. 2673 (3) (2019) 365–374.
[16] P. Singhvi, et al., Impacts of field and laboratory long-term aging on asphalt binders, Transp. Res. Rec. (2022), p. 03611981221083614.
[17] S. Khalighi, et al., Multivariate chemo-rheological framework for optimizing laboratory aging protocols of paving binders, Mater. Des. (2024) 113520.
[18] I. Menapace, W. Yiming, E. Masad, Effects of environmental factors on the chemical composition of asphalt binders, Energy Fuels 33 (4) (2018) 2614–2624.
[19] J. Crucho, et al., Tecnico accelerated ageing (TEAGE)–a new laboratory approach for bituminous mixture ageing simulation, Int. J. Pavement Eng. 21 (6) (2020) 753–765.
[20] S. Wu, et al., UV and thermal aging of pure bitumen-comparison between laboratory simulation and natural exposure aging, Road. Mater. Pavement Des. 9 (sup1) (2008) 103–113.
[21] J. Hu, et al., Effect of ultraviolet radiation in different wavebands on bitumen, Constr. Build. Mater. 159 (2018) 479–485.
[22] A.S. Lopes, et al., Impact of aging protocols on asphalt binder behavior: a laboratory and field study, Case Stud. Constr. Mater. 19 (2023) e02629.
[23] J. Mirwald, et al., Impact of UV–Vis light on the oxidation of bitumen in correlation to solar spectral irradiance data, Constr. Build. Mater. 316 (2022) 125816.
[24] C.V. Singh, et al., Formation of functionally graded hybrid composite materials with Al2O3 and RHA reinforcements using friction stir process, Aust. J. Mech. Eng. 20 (1) (2022) 141–154.
[25] D.J. Jacob, Heterogeneous chemistry and tropospheric ozone, Atmos. Environ. 34 (12-14) (2000) 2131–2159.
[26] J. Mirwald, et al., Impact of reactive oxygen species on bitumen aging–The Viennese binder aging method, Constr. Build. Mater. 257 (2020) 119495.
[27] B. Hofko, et al., Bitumen ageing–Impact of reactive oxygen species, Case Stud. Constr. Mater. 13 (2020) e00390.
[28] K. Hofer, et al., Influence of selected reactive oxygen species on the long-term aging of bitumen, Mater. Struct. 55 (5) (2022) 133.
[29] S. Khalighi, S. Erkens, A. Varveri, Exploring the impact of humidity and water on bituminous binder aging: a multivariate analysis approach (TI CAB), Road. Mater. Pavement Des. (2024) 1–25.
[30] T. López-Montero, R. Miró, Differences in cracking resistance of asphalt mixtures due to ageing and moisture damage, Constr. Build. Mater. 112 (2016) 299–306.
[31] HUANG, S.-C., T. Turner, and K. Thomas. The influence of moisture on the aging characteristics of bitumen. in PROCEEDINGS OF THE 4TH EURASPHALT AND EUROBITUME CONGRESS HELD MAY 2008, COPENHAGEN, DENMARK. 2008.
[32] J.C. Mierzwa, R. Rodrigues, A.C. Teixeira, UV-hydrogen peroxide processes. Advanced oxidation processes for waste water treatment, Elsevier, 2018, pp. 13–48.
[33] G. Boczkaj, A. Fernandes, P. Makoś, Study of different advanced oxidation processes for wastewater treatment from petroleum bitumen production at basic pH, Ind. Eng. Chem. Res. 56 (31) (2017) 8806–8814.
[34] M. Rodríguez-Peña, et al., New insights about the electrochemical production of ozone, Curr. Opin. Electrochem. 27 (2021) 100697.
[35] S. Gligorovski, et al., Environmental implications of hydroxyl radicals (• OH), Chem. Rev. 115 (24) (2015) 13051–13092.
[36] Khalighi, S., et al., The Impact of Reactive Oxygen Species Coupled with Moisture on Bitumen Long-Term Aging. 2024.
[37] L. Porot, et al., Fourier-transform infrared analysis and interpretation for bituminous binders, Road. Mater. Pavement Des. 24 (2) (2023) 462–483.
[38] Khalighi, S., et al., Evaluating the Impact of Data Pre-Processing Methods on Classification of Atr-Ftir Spectra of Bituminous Binders. Available at SSRN 4852406.
[39] R. Jing, et al., Ageing effect on chemo-mechanics of bitumen, Road. Mater. Pavement Des. 22 (5) (2021) 1044–1059.
[40] 14770, E., Bitumen and bituminous binders–Determination of complex shear modulus and phase angle using a Dynamic Shear Rheometer (DSR). 2012, European Committee for Standardization Brussels.
[41] M. Domazet-Lošo, B. Haubold, Efficient estimation of pairwise distances between genomes, Bioinformatics 25 (24) (2009) 3221–3227.
[42] M. Asemani, A.R. Rabbani, Detailed FTIR spectroscopy characterization of crude oil extracted asphaltenes: curve resolve of overlapping bands, J. Pet. Sci. Eng. 185 (2020) 106618.
[43] M. Müller, Dynamic time warping, Inf. Retr. Music Motion (2007) 69–84.
[44] J. Zhang, et al., Defect identification of layered adhesive structures based on dynamic time warping and simulation analysis, Infrared Phys. Technol. 120 (2022) 103943.
[45] K. Li, et al., Using dynamic time warping self-organizing maps to characterize diurnal patterns in environmental exposures, Sci. Rep. 11 (1) (2021) 24052.
[46] J. Mirwald, et al., Understanding bitumen ageing by investigation of its polarity fractions, Constr. Build. Mater. 250 (2020) 118809.
[47] S. Khalighi, L. Ma, A. Varveri, Accelerated laboratory simulations to mimic field aging of bituminous binders and mixtures: A multivariant analysis on environmental aging effects2024, ⟨https://ssrn.com/abstract=4995141⟩.
[48] M. Scarsella, et al., Petroleum heavy ends stability: evolution of residues macrostructure by aging, Energy fuels 13 (3) (1999) 739–747.
[49] R. Jing, et al., Rheological, fatigue and relaxation properties of aged bitumen, Int. J. Pavement Eng. 21 (8) (2020) 1024–1033.